

Unbiased Cosmology Inference from Biased Tracers using the EFT Likelihood

Fabian Schmidt,^a Giovanni Cabass,^a Jens Jasche,^b and Guilhem Lavaux^c

^aMax-Planck-Institut für Astrophysik, Karl-Schwarzschild-Straße 1, 85748 Garching, Germany

^bThe Oskar Klein Centre, Department of Physics, Stockholm University, Albanova University Center, SE 106 91 Stockholm, Sweden

^cSorbonne Université, CNRS, UMR 7095, Institut d'Astrophysique de Paris, 98 bis bd Arago, 75014 Paris, France

E-mail: fabians@mpa-garching.mpg.de, gcabass@mpa-garching.mpg.de, jens.jasche@fysik.su.se, guilhem.lavaux@iap.fr

Abstract. We present updates on the cosmology inference using the effective field theory (EFT) likelihood presented previously in Schmidt et al., 2018, Elsner et al., 2019 [1, 2]. Specifically, we add a cutoff to the initial conditions that serve as starting point for the matter forward model. We show that this cutoff, which was not employed in any previous related work, is important to regularize loop integrals that otherwise involve small-scale, non-perturbative modes. We then present results on the inferred value of the linear power spectrum normalization σ_8 from rest-frame halo catalogs using both second- and third-order bias expansions, imposing uniform priors on all bias parameters. Due to the perfect bias- σ_8 degeneracy at linear order, constraints on σ_8 rely entirely on nonlinear information. The results show the expected convergence behavior when lowering the cutoff in wavenumber, Λ . When including modes up to $k \leq \Lambda = 0.1 h \text{ Mpc}^{-1}$ in the second-order case, σ_8 is recovered to within $\lesssim 6\%$ for a range of halo masses and redshifts. The systematic bias shrinks to 4% or less for the third-order bias expansion on the same range of scales. Together with additional evidence we provide, this shows that the residual mismatch in σ_8 can be attributed to higher-order bias contributions. We conclude that the EFT likelihood is able to infer unbiased cosmological constraints, within expected theoretical systematic errors, from physical biased tracers on quasilinear scales.

Keywords: cosmological parameters from LSS, redshift surveys, dark matter halos, bias, effective field theory

ArXiv ePrint: [2004.06707](https://arxiv.org/abs/2004.06707)

Contents

1	Introduction	1
2	The EFT likelihood	3
3	The cutoff on the initial conditions and the maximum-a-posteriori point	5
4	Numerical implementation	13
5	Results	15
5.1	Test on N-body particles	15
5.2	Second-order bias	16
5.3	Third-order bias	21
5.4	Halo density field	24
6	Conclusions	25
A	Deriving the maximum-a-posteriori relation	28
B	Maximum-a-posteriori relation for $O = O' = \delta$	28
C	Fourier-Taylor density assignment	31

1 Introduction

State-of-the-art approaches for the analysis of large-scale structure (LSS) data typically make use of summary statistics like the two-point correlation function to compare theoretical models to observational data. Alternative approaches have been developed however that take a more ambitious avenue to cosmological signal inference. Instead of focusing on summary statistics, they aim directly at reconstructing the three-dimensional underlying matter density field from observations of astrophysical tracers like galaxies [3–17] (see [18–20] for closely related approaches).

The general approach works as follows. Starting from a set of initial conditions at high redshift, drawn from a multivariate Gaussian distribution consistent with the measurements of cosmic microwave background radiation experiments, nonlinear effects of gravitational collapse are taken into account via approximate semi-analytical or numerical methods to compute the corresponding evolved density field at low redshift that is to be compared to observations. Then, one samples the initial conditions, as well as cosmological and nuisance parameters, to obtain the desired posterior for the initial phases and cosmological parameters given the observed density field.

However, what we observe is not the evolved matter density field itself, but rather biased tracers of this field such as galaxies, quasars, galaxy clusters, the Lyman- α forest, and others (see [21] for a review). These are complex nonlinear objects whose formation happens over long time scales and involves extremely small-scale physical processes compared to cosmological length scales. The effective field theory (EFT) of LSS allows for a controlled incorporation of the effects of fully nonlinear structure formation on small scales in the

framework of cosmological perturbation theory [22, 23]. This is especially important when attempting to infer cosmological information from observed biased tracers, since we currently have no way of simulating the formation of such tracers from first principles, at least not to the required accuracy. Hence, approaches which rigorously abstract from this imperfect knowledge of the small-scale processes involved in the formation of observed tracers are highly valuable.

While the calculation of galaxy clustering observables in the EFT has largely been restricted to correlation functions so far, Refs. [1, 24] recently presented a derivation of the likelihood of the entire galaxy density field $\delta_g(\mathbf{x}, \tau) = n_g(\mathbf{x}, \tau)/\bar{n}_g(\tau) - 1$ given the nonlinear, evolved matter density field, in the context of the EFT. Here, $n_g(\mathbf{x}, \tau)$ is the comoving rest-frame galaxy density, while $\bar{n}_g(\tau)$ denotes its time-dependent mean. This result offers several advantages over the previous results restricted to correlation functions, among them the fact that it does not rely on a perturbative expansion of the matter density field. Rather, the likelihood is given in terms of the fully nonlinear density field, which can be predicted for example using N-body simulations, and thus isolates the truly uncertain aspects of the observed galaxy density. This conditional likelihood of the galaxy density field given the evolved matter density field is precisely the key ingredient required in the Bayesian inference approaches mentioned above, and can be employed there directly [1, 2].

Our goal for this paper, as a followup to [2], is to demonstrate unbiased inference of the linear matter power spectrum normalization σ_8 from halo catalogs in real space.¹ The degeneracy between the linear bias b_1 and σ_8 , which is perfect in linear theory, can be broken when including nonlinear information, even when marginalizing over all relevant nonlinear bias terms. In particular, the fact that the displacement term contained in the second-order matter density is also multiplied by b_1 , coupled with the fact that the second-order matter density scales differently with σ_8 than the linear-order one, breaks the degeneracy. Thus, fundamentally, the possibility of estimating σ_8 in this way is due to the equivalence principle, which ensures that galaxies move on the same trajectories as matter on large scales; that is, the equivalence principle requires that the second-order displacement term is multiplied by the same bias coefficient as the linear-order density field (see also Sec. 2 of [21]). At higher orders in perturbations, such as when going to third order, more terms that are protected by the equivalence principle appear, and the EFT likelihood will consistently capture those as well [24].

The results presented in [2] however showed a residual bias in the inferred σ_8 value that was on the order of 10 %–20 %. Here, we present a key modification in the construction of the likelihood presented in [2] in form of a cutoff Λ_{in} applied in the initial conditions in Fourier space, and show that this lowers the bias in the inferred σ_8 value by a factor of several. Moreover, it restores the expected convergence behavior as a function of the cutoff scale. We also extend the bias expansion to third order, which further improves the accuracy in the determination of σ_8 significantly, again demonstrating the expected convergence behavior of the EFT when applied on scales where perturbation theory is valid.

The paper is organized as follows. In Sec. 2 we briefly review the statistical framework to analyze LSS data developed in [1, 2], which forms the basis of our analysis. We then discuss the significance of the cutoff in the initial conditions for the EFT likelihood in Sec. 3.

¹Strictly speaking, we are really performing an inference of the primordial amplitude \mathcal{A}_s , rather than σ_8 . However, to conform with standard convention in the LSS literature as well as the previous papers in this series, we continue to use σ_8 . The conversion between the two parameters is unambiguous since we keep all other cosmological parameters fixed.

After describing the numerical implementation in Sec. 4, we turn to the results in Sec. 5. We conclude in Sec. 6. The appendices contain some additional calculations and implementation details relevant for Sec. 3 and Sec. 4.

2 The EFT likelihood

The full posterior for cosmological parameters given an observed density of biased tracers is obtained by marginalizing the likelihood $P(\delta_h|\delta_{\text{in}},\theta,\{b_O,\sigma_a\})$ of observing the density field² δ_h given the initial conditions δ_{in} , and cosmological as well as nuisance parameters (θ and $\{b_O,\sigma_a\}$, respectively), over the initial phases of the matter density field, weighted by the Gaussian prior for the latter. The physics of the formation and evolution of biased tracers is contained in the likelihood $P(\delta_h|\delta_{\text{in}},\theta,\{b_O,\sigma_a\})$, which can be broken down into three components:

1. The deterministic forward model for matter, $\delta_{\text{fwd}}[\delta_{\text{in},\Lambda_{\text{in}}}]$. In this paper, we show results for two forward models: second-order Lagrangian perturbation theory (2LPT), and full N-body simulations. Crucially, and in contrast to the results presented in [1, 2], initial density perturbations with wavenumbers $k > \Lambda_{\text{in}}$, where Λ_{in} is an initial cutoff, are set to zero. We denote the resulting filtered initial density field as $\delta_{\text{in},\Lambda_{\text{in}}}$. We return to this in Sec. 3.
2. The bias relation, which yields the prediction for the halo density field in a mean-field sense, which we write as

$$\delta_{h,\text{det}}(\mathbf{x}) = \sum_O b_O O[\delta_\Lambda](\mathbf{x}) , \quad (2.1)$$

where the set of operators is ranked according to orders in perturbations and spatial derivatives, following the general bias expansion or equivalently EFT approach [21, 25, 26]. Note that the bias expansion accounts for the time evolution (formation history) of tracers, even though it is written at a fixed time. This is possible by virtue of including operators corresponding to convective time derivatives, and by restricting to a fixed order in perturbation theory (see Sec. 2.5 of [21]). In Eq. (2.1), $\delta = \delta_{\text{fwd}}[\delta_{\text{in},\Lambda_{\text{in}}}]$ is obtained from the forward model for matter, and δ_Λ denotes the sharp- k filtered version of δ , where all modes with $k > \Lambda$ are set to zero. Notice that the filter is applied *before* constructing the bias fields O . In this paper, we will use second- and third-order bias expansions, as explained later in this section. Throughout, we drop the time argument on fields for clarity. All fields, including halos, operators, and matter density, are evaluated at the same epoch here.

3. The distribution of the likelihood around the mean-field halo density field, which, as derived in [1, 24], can be written as a Gaussian in Fourier space with diagonal covariance that is given as a power series in k^2 . Specifically, we have

$$\ln P(\delta_h|\delta,\{b_O,\sigma_a\}) = -\frac{1}{2} \sum_{\mathbf{k} \neq 0}^{k_{\text{max}}} \left[\ln[2\pi\sigma^2(k)] + \frac{1}{\sigma^2(k)} |\delta_h(\mathbf{k}) - \delta_{h,\text{det}}[\delta,\{b_O\}](\mathbf{k})|^2 \right] . \quad (2.2)$$

²Since our numerical results below are for halos, we refer to the data as $\delta_h \equiv n_h/\bar{n}_h - 1$ throughout; the general approach described in this section applies to any LSS tracer however.

We parametrize $\sigma^2(k)$ as

$$\sigma^2(k) = \left(\sigma_\varepsilon + k^2 \sigma_{\varepsilon,2} \right)^2 . \quad (2.3)$$

The parametrization is chosen so that $\sigma^2(k)$ is positive definite. σ_ε^2 can be interpreted as the amplitude of halo stochasticity in the large-scale limit ($k \rightarrow 0$). $\sigma_{\varepsilon,2}^2$ is the leading scale-dependent correction to the halo stochasticity. This term scales as k^2 , rather than some lower power of k , since it captures the backreaction of small physical scales in real space, and thus has to correspond to a local operator in real space (see Sec. 2.7 of [21] for a discussion).³ In fact, we find that the inclusion of $\sigma_{\varepsilon,2}$ has a negligible impact on our results.

In the actual implementation, all fields are discretized on a uniform cubic grid. We employ the discrete Fourier transform in our equations, so that fields in Fourier space are dimensionless as well. In the following, we will refer to the conditional probability in Eq. (2.2) simply as “likelihood,” since it is the part of the overall likelihood of biased tracers that is relevant for the study presented in this paper.

The likelihood involves, in principle, all three distinct cutoffs, Λ_{in} , Λ [Eq. (2.1)], and k_{max} [Eq. (2.2)], that we introduced in points 1 to 3 of the previous paragraph, respectively. From the EFT perspective, the cutoff Λ_{in} on the initial conditions is the relevant scale [24, 28], while the latter two are choices made in the numerical implementation. In this paper, we will set $k_{\text{max}} = \Lambda = \Lambda_{\text{in}}$ throughout. We return to this in Sec. 5.

Following Ref. [1], we show results for the bias expansion up to second order in perturbations, i.e., we restrict ourselves to the following set of bias operators:

$$O \in \{ \delta, \delta^2, K^2, \nabla^2 \delta \} , \quad (2.4)$$

where δ is the fractional matter density perturbation, and

$$K^2 \equiv (K_{ij})^2 = \left(\left[\frac{\partial_i \partial_j}{\nabla^2} - \frac{1}{3} \delta_{ij} \right] \delta \right)^2 \quad (2.5)$$

is the tidal field squared. The corresponding bias parameters are denoted as b_O ; we also denote $b_1 \equiv b_\delta$.

We have also extended our bias model to third order, in which case the set of bias operators now comprises

$$O \in \{ \delta, \delta^2, K^2, \nabla^2 \delta, \delta^3, \delta K^2, K^3, O_{\text{td}} \} , \quad (2.6)$$

where

$$O_{\text{td}} \equiv \frac{8}{21} K_{ij} \frac{\partial_i \partial_j}{\nabla^2} \left(\delta^2 - \frac{3}{2} K^2 \right) . \quad (2.7)$$

At third order, this operator can be interpreted in a variety of different ways, for example as the convective time derivative of the tidal field squared, or the difference between tidal and velocity shear (see Sec. 2.4 of [21]).

³As argued in [24, 27] the higher-derivative stochastic term is actually subleading compared to the modulation of the stochasticity by large-scale density perturbations; however, even the latter is less relevant than any of the deterministic bias terms that we include, which go up to third order. We leave an exploration of the field-dependent stochasticity to future work.

Notice that the bias expansion Eq. (2.1) is an expansion in two small parameters, essentially in perturbations and spatial derivatives (see Sec. 4.1 of [21] for a detailed discussion). In Eq. (2.4) and Eq. (2.6), we assume that both small parameters are comparable, which leads us to include terms up to second or third order in perturbations, as well as the leading higher-derivative operator $\nabla^2\delta$ in Eq. (2.4). The reasoning behind this is discussed in greater detail in [1]. We emphasize that it is extremely simple to add additional higher-derivative bias terms in the EFT likelihood, and numerically efficient as well once the analytical marginalization over bias parameters is employed following the procedure described in [2].

For all results apart from those in Sec. 5.4, we marginalize over all bias parameters apart from b_1 analytically. In the second-order bias case, we thus marginalize over three parameters, while in the third-order case, the marginalization is over seven parameters. This substantially speeds up the numerical search for the maximum-likelihood point, since, for either bias expansions, the parameter set is reduced to $\{b_O, \sigma_a\} \rightarrow \{b_1, \sigma_\varepsilon, \sigma_{\varepsilon,2}\}$.

Ref. [1] describes a renormalization procedure for the operators that ensures that their coefficients match the bias parameters that would be inferred from the large-scale statistics of halos, such as the power spectrum and bispectrum. Since the results on σ_8 which we focus on in this paper are independent of the renormalization, we do not employ it here.

One important difference in Eq. (2.3) as compared to that presented in [1, 2] is the removal of the term $b_1\sigma_{\varepsilon\varepsilon_m,2}k^2$ in $\sigma^2(k)$. This would represent, at the level of correlation functions, the leading contribution to the halo-matter power spectrum that is analytic in k^2 . As long as uniform priors are employed on the parameters b_1 and $\sigma_{\varepsilon,2}$, this term can be absorbed by a b_1 -dependent redefinition of $\sigma_{\varepsilon,2}$ and thus does not influence the maximum-likelihood point. As we show in Appendix B, the use of a cutoff in the initial conditions in fact removes the justification for this term that was put forward in [1].

To summarize, the differences to the likelihood presented in [1, 2] are (i) the use of a cutoff Λ_{in} in the initial conditions; (ii) the removal of a b_1 -dependent term in the variance of the likelihood Eq. (2.2); (iii) the extension of the bias expansion to third order.

As for the results reported in [1, 2], we do not sample the initial phases but rather fix them to the values used to initialize the N-body simulations within which the halos were identified. Since this removes cosmic variance to the largest extent possible, and thus shrinks the error bars significantly over the case where phases are allowed to vary, this is likely to be the most stringent possible test of the conditional likelihood $P(\delta_h|\delta, \{b_O, \sigma_a\})$. We use the profile likelihood [29] introduced in [2] in order to estimate the maximum-likelihood value for σ_8 . For a probability distribution $P(\sigma_8, \{b_1, \sigma_a\}|\delta_h)$, the profile likelihood for the parameter σ_8 is defined as the maximum probability within the parameter space that is being profiled over:

$$P^{\text{prof}}(\sigma_8) = \max_{\{b_1, \sigma_a\}} [P(\sigma_8, \{b_1, \sigma_a\}|\delta_h)] . \quad (2.8)$$

Here, the set of parameters $\{b_1, \sigma_a\}$ has been profiled out. In practice, we interpolate the profile likelihood evaluated on a predefined grid in σ_8 centered about the fiducial value of the simulation. The details of this procedure are the same as described in [2].

3 The cutoff on the initial conditions and the maximum-a-posteriori point

The main change to the EFT likelihood implementation presented here over the previous results in [1, 2] is the imposition of a wavenumber (or momentum) cutoff in the initial conditions. Let us now discuss the significance of this cutoff.

In order to determine whether the EFT likelihood in Eq. (2.2) leads to unbiased estimates of the parameters of interest, which in the present case are σ_8 and the set of bias parameters, we study the maximum-a-posteriori (MAP) relation of the likelihood at fixed phases. Since the likelihood depends nonlinearly on the phases (via the forward model δ_{fwd} as well as the nonlinear bias operators), it is extremely difficult to study the likelihood with varying phases analytically. Fortunately, the *ensemble average over the phases of the fixed-phase MAP* relation can be derived analytically [1]; this is summarized in Appendix A. This relation is the relevant quantity to compare with the MAP value of σ_8 obtained below in the application to halos in N-body simulations, which should follow the analytical relation in the limit of infinite simulation volume (to the precision of perturbation theory at the order and value of the cutoff considered).

We can in fact further restrict to the MAP relation for the bias parameters. The relation for σ_8 can be obtained via a generalization of this relation, since each term in the likelihood has a definite scaling with σ_8 in the context of perturbation theory [1]. Taking the derivative of the logarithm of the likelihood with respect to a bias parameter b_O , and neglecting any priors on the bias parameters, we obtain (Appendix A):

$$\sum_{\mathbf{k} \neq 0}^{k_{\text{max}}} \frac{1}{\sigma^2(k)} \langle \delta_h(\mathbf{k}) O(\mathbf{k}') \rangle = \sum_{\mathbf{k} \neq 0}^{k_{\text{max}}} \frac{1}{\sigma^2(k)} \sum_{O'} b_{O'} \langle O'(\mathbf{k}) O(\mathbf{k}') \rangle \quad \forall O, \quad (3.1)$$

where the sum runs over all operators in the deterministic bias expansion. As discussed above, and shown in [1], these relations need to be fulfilled in order to ensure an unbiased inference of cosmological parameters and in particular σ_8 .

The left-hand side of Eq. (3.1) involves the cross-correlation of the data, δ_h , with an operator constructed from the forward-evolved density, O , while the right-hand side only involves operators constructed from the forward-evolved density field. Both sides can be evaluated, to a given order in perturbations, by means of the EFT of large-scale structure, which allows us to establish whether the construction of the likelihood in fact leads to unbiased inference. Each side contains loop integrals which come from three sources of nonlinearities: the nonlinear forward model for matter, the nonlinearity in the bias operators, and the nonlinear evolution of the actual halos, which enters on the left-hand side. Thus, establishing the identity Eq. (3.1) is not trivial. In the following, we study the properties of these loop integrals in detail, and show under what conditions the MAP relation holds within the EFT. In this section, we present general derivations; concrete examples for specific operators are given in Appendix B.

Restricting Eq. (3.1) to a single $k < k_{\text{max}}$ to be specific, we thus have

$$\langle \delta_h(\mathbf{k}) O(\mathbf{k}') \rangle = \sum_{O'} b_{O'} \langle O'(\mathbf{k}) O(\mathbf{k}') \rangle \quad \forall O. \quad (3.2)$$

Notice that we expect the EFT approach to apply for any shape of the linear power spectrum (although the reach of perturbation theory will depend on this shape). For this reason, it is necessary that the equality Eq. (3.2) hold for individual k . Our goal is to investigate this relation in the context of perturbation theory. Thus, we expand the halo density field in a set of renormalized bias operators, multiplied by bias coefficients [21]:

$$\delta_h(\mathbf{k}) = \sum_O b_O^h [O](\mathbf{k}). \quad (3.3)$$

Notice the crucial difference between the operators $[O]$ appearing here and those appearing explicitly in Eq. (3.2). The former are assumed to be constructed from the evolved density field without any cutoffs:

$$[O] = [O[\delta_\infty]] , \quad (3.4)$$

where δ_∞ denotes the full forward-evolved density field without cutoffs. That is, halos in regular N-body simulations, or actual observed galaxies, evolve together with the nonlinear matter distribution without any cutoffs on the initial or final density fields imposed. On the other hand, the operators appearing in the likelihood are constructed from the filtered evolved density field

$$O = O[\delta_\Lambda] , \quad \text{where} \quad \delta_\Lambda(\mathbf{k}) = W_\Lambda(\mathbf{k})\delta_{\text{fwd}}[\delta_{\text{in},\Lambda_{\text{in}}}](\mathbf{k}) \quad (3.5)$$

is the evolved density field filtered on the scale Λ , starting from initial conditions $\delta_{\text{in},\Lambda_{\text{in}}}$ *filtered on the scale Λ_{in}* . The effect of removing this cutoff can be obtained by sending $\Lambda_{\text{in}} \rightarrow \infty$. In all cases, we adopt an isotropic sharp- k filter,

$$W_\Lambda(\mathbf{k}) \equiv \Theta_H(\Lambda - |\mathbf{k}|) , \quad (3.6)$$

where Θ_H is the Heaviside function.

We assume that the set of operators are linearly independent, and that they form a complete basis of local observables at a given order in perturbation theory and derivatives (this is the case for the list of operators in Eq. (2.4) and Eq. (2.6) for example). In order for Eq. (3.2) to hold for *any* tracer, it thus has to hold individually for all bias operators O and O' . This finally leads us to compare the two correlators

$$\langle [O'[\delta_\infty]](\mathbf{k})O[\delta_\Lambda](\mathbf{k}') \rangle \quad \text{and} \quad \langle O'[\delta_\Lambda](\mathbf{k})O[\delta_\Lambda](\mathbf{k}') \rangle . \quad (3.7)$$

The correlator on the left can be written as

$$\begin{aligned} \langle [O'[\delta_\infty]](\mathbf{k})O[\delta_\Lambda](\mathbf{k}') \rangle &= \int_{\mathbf{p}_1, \dots, \mathbf{p}_n} S_{O'}(\mathbf{p}_1, \dots, \mathbf{p}_n) (2\pi)^3 \delta_D^{(3)}(\mathbf{k} - \mathbf{p}_{1\dots}) \\ &\times \int_{\mathbf{p}'_1, \dots, \mathbf{p}'_m} S_O^\Lambda(\mathbf{p}'_1, \dots, \mathbf{p}'_m) (2\pi)^3 \delta_D^{(3)}(\mathbf{k}' - \mathbf{p}'_{1\dots}) \langle \delta_\infty(\mathbf{p}_1) \cdots \delta_\infty(\mathbf{p}_n) \delta_{\text{fwd}}(\mathbf{p}'_1) \cdots \delta_{\text{fwd}}(\mathbf{p}'_m) \rangle \\ &+ \text{counterterms} , \end{aligned} \quad (3.8)$$

where we have taken O' (O) to be constructed out of n (m) density fields. We will frequently denote this as $O' = O'^{[n]}$ ($O = O^{[m]}$). The kernels S_O , $S_{O'}$ are specific to each operator; for example for the operators in the list Eq. (2.4) we have⁴

$$S_\delta(\mathbf{p}) = 1; \quad S_{\delta^2}(\mathbf{p}_1, \mathbf{p}_2) = 1; \quad S_{K^2}(\mathbf{p}_1, \mathbf{p}_2) = \frac{(\mathbf{p}_1 \cdot \mathbf{p}_2)^2}{p_1^2 p_2^2} - \frac{1}{3}; \quad S_{\nabla^2 \delta}(\mathbf{p}) = -p^2. \quad (3.9)$$

Further, we have defined the kernels with cutoff as

$$S_O^\Lambda(\mathbf{p}_1, \dots, \mathbf{p}_n) \equiv W_\Lambda(\mathbf{p}_1) \cdots W_\Lambda(\mathbf{p}_n) S_O(\mathbf{p}_1, \dots, \mathbf{p}_n), \quad (3.10)$$

⁴In general, the kernels for bias operators at leading order in derivatives are homogeneous (of degree 0), rational functions of linear combinations of the momenta. Kernels for higher-derivative operators are homogeneous with degrees 2, 4, ...

and denoted $\mathbf{p}_{1\dots n} \equiv \mathbf{p}_1 + \dots + \mathbf{p}_n$. Finally, we continue to denote the evolved matter density field without any cutoffs as δ_∞ , while δ_{fwd} denotes the matter density field evolved with a cutoff Λ_{in} in the initial conditions, cf. Eq. (3.5). The last line in Eq. (3.8) contains the counterterms which we will discuss below. The second correlator in Eq. (3.7) follows an analogous expression, with $S_{O'} \rightarrow S_{O'}^\Lambda$ and $\delta_\infty(\mathbf{p}_i) \rightarrow \delta_{\text{fwd}}(\mathbf{p}_i)$, and no counterterms. Due to the cutoffs Λ and Λ_{in} , this correlator only involves modes with momenta (wavenumbers) of order $\Lambda, \Lambda_{\text{in}}$ or less.

The unfiltered density fields appearing in $[O'[\delta_\infty]]$ lead to loop integrals whose momenta run to infinity. These need to be regularized by adding counterterms [25, 26, 30], which we can describe at the level of the operators as consisting of linear combinations of equal- or lower-order operators \tilde{O} which are subtracted:

$$[O'](\mathbf{k}) = O'(\mathbf{k}) - \sum_{\tilde{O}} \sigma_{O',\tilde{O}}^2 \tilde{O}(\mathbf{k}) , \quad (3.11)$$

where the constants $\sigma_{O',\tilde{O}}^2$ involve loop integrals (as well as finite contributions in general), and can have either sign. Inserting this relation into Eq. (3.8), it is then clear that the counterterms on the last line can be described in terms of similar correlators as the first, “bare” contribution. Specifically, Ref. [30] argued that renormalization should ensure that correlators involving $[O']$ and l linear density fields $\delta^{(1)}(\mathbf{p}_1), \dots, \delta^{(1)}(\mathbf{p}_l)$ asymptote to tree-level results as the external momenta become small (see also Sec. 2.10 of [21] for an extended discussion):

$$\lim_{\{p_i\} \rightarrow 0} \frac{\langle [O'](\mathbf{k}) \delta^{(1)}(\mathbf{p}_1) \dots \delta^{(1)}(\mathbf{p}_l) \rangle}{\langle O'(\mathbf{k}) \delta^{(1)}(\mathbf{p}_1) \dots \delta^{(1)}(\mathbf{p}_l) \rangle_{\text{LO}}} = 1 , \quad (3.12)$$

where $l = 1, 2, \dots$, and the subscript on the correlator in the denominator indicates the leading-order (LO) expression in perturbation theory. Notice that, for $l = n$, this correlator is directly related to the kernel $S_{O'}$ through

$$\langle O'^{[n]}(\mathbf{k}) \delta^{(1)}(\mathbf{p}_1) \dots \delta^{(1)}(\mathbf{p}_n) \rangle'_{\text{LO}} = n! S_{O'}(\mathbf{p}_1, \dots, \mathbf{p}_n) P_{\text{L}}(p_1) \dots P_{\text{L}}(p_n) , \quad (3.13)$$

where a prime on a correlator denotes that the momentum-conserving Dirac delta is removed, and we have assumed that the kernel $S_{O'}$ is fully symmetrized in its arguments. In the following, we will work with the linearly evolved density field $\delta^{(1)}(\mathbf{p}) \propto \delta_{\text{in}}(\mathbf{p})$ instead of δ_{in} itself, as is common in perturbation-theory calculations, where the two fields are simply related by the linear growth factor.

The first correlator in Eq. (3.7) can be represented diagrammatically as

$$\begin{aligned}
\langle [O'[\delta_\infty]](\mathbf{k}) O[\delta_\Lambda](\mathbf{k}') \rangle = & \text{Diagram 1} \\
& + \text{Diagram 2} + \text{higher-order counterterms} ,
\end{aligned} \tag{3.14}$$

where the first diagram gives the contribution of the first two lines of Eq. (3.8), while the second illustrates one of the counterterms, more precisely the one where \tilde{O} is equal to δ in Eq. (3.11).

In the following, we will consider specific cases in diagrammatic form. Let us thus state the relevant Feynman rules:

1. We employ the same notation as adopted in [31] and App. B of [21]. The external vertices $S_O, S_{O'}$ are denoted as squares; for an n -th order operator, the corresponding vertex has n ingoing lines and 1 outgoing line. The perturbation-theory kernels F_n (see [32]) are denoted as open circles, likewise with n ingoing and a single outgoing line. Each vertex further contains a momentum-conserving Dirac delta (e.g., $(2\pi)^3 \delta_D^{(3)}(\mathbf{k} - \mathbf{p}_{1\dots n})$ in case of the $S_{O'}$ vertex).
2. Two types of linear power spectra appear: those without cut, $P_L(p)$ (denoted with a dot), and those cut at Λ_{in} , $W_{\Lambda_{\text{in}}}(p)P_L(p)$ (denoted with a crossed circle). The rule governing which to choose is that *any linear power spectrum connected to a final outgoing line going to the right* (i.e. toward S_O^Λ) is cut at Λ_{in} . If a power spectrum is only connected to outgoing lines ending up on the left (i.e. at $S_{O'}$), then it is not cut. This follows from the fact that the outgoing lines connecting to the right correspond to evolved fields with an initial-condition cutoff, and that $\langle \delta_\infty^{(1)} \delta_{\Lambda_{\text{in}}}^{(1)} \rangle' = \langle \delta_{\Lambda_{\text{in}}}^{(1)} \delta_{\Lambda_{\text{in}}}^{(1)} \rangle' = W_{\Lambda_{\text{in}}} P_L$.
3. Any unregularized loop integral appearing in a diagram for an n -th order operator O' on the left is to be removed by a corresponding counterterm for the operator O' , whose vertex we denote by a crossed square (in the following diagrams we will omit the labels on these vertices for simplicity of notation). The counterterm is obtained by cutting at most n soft lines in the diagram (i.e. lines with momenta at most of order Λ , Λ_{in}).

The rule for the identification of counterterms is equivalent to the renormalization conditions in Eq. (3.12), since it isolates loop integrals that are fully connected with the left-hand side of the diagram, i.e. with $S_{O'}$, in the same way as Eq. (3.12) ensures that loops are fully connected with O' by considering only correlators of the operator with powers of $\delta^{(1)}$.

However, here we will only include loop momenta above Λ_{in} in our counterterms, since the contribution from modes below the cutoff is matched by the corresponding correlator involving $O'[\delta_\Lambda]$ in Eq. (3.7). Thus, the counterterms given below differ by a finite contribution from those commonly defined when computing correlation functions, which can be interpreted as adopting a different renormalization scale (Λ_{in} rather than the large-scale limit 0).

Let us now consider the lowest-order operator correlators, evaluating each of them up to next-to-leading order (NLO, or 1-loop). This will involve diagrams including up to three linear power spectra. Let us begin with $O' = O = \delta$, such that $S_{O'} = 1$ and $S_O^\Lambda(\mathbf{k}) = W_\Lambda(k)$, corresponding to the correlator $\langle \delta_\infty(\mathbf{k}) \delta_\Lambda(\mathbf{k}') \rangle$. The diagrams are

where F_2 and F_3 are the second- and third-order perturbation-theory kernels, respectively (in the following diagrams we will omit the label on the perturbation-theory kernels for simplicity of notation). There are three NLO contributions, only one of which has a loop integral that runs to infinity; the others are regularized by Λ_{in} . It is straightforward to see that the counterpart of this correlator in the MAP relation, i.e. the right correlator in Eq. (3.7) $\langle \delta_\Lambda(\mathbf{k}) \delta_\Lambda(\mathbf{k}') \rangle$, differs only through this loop contribution, which instead of being unregularized is now also regularized by Λ_{in} . The unregularized loop integral, and hence the mismatch between the correlators in Eq. (3.7) for $O' = O = \delta$, is to be absorbed by a counterterm to $[\delta]$, corresponding to the part of the diagram left of the dotted line, so that

$$[\delta](\mathbf{k}) = \left[1 - 3 \int_{|\mathbf{p}| > \Lambda_{\text{in}}} F_3(\mathbf{p}, -\mathbf{p}, \mathbf{k}) P_L(p) - C_s^2(\Lambda_{\text{in}}) \frac{k^2}{k_{\text{NL}}^2} \right] \delta(\mathbf{k}) , \quad (3.16)$$

where the second term absorbs the loop integral while the last term is the finite contribution of unknown size, whose coefficient is the effective sound speed of matter C_s^2 [22, 23], defined with respect to the scale Λ_{in} . Here, k_{NL} is the nonlinear scale defined through $k_{\text{NL}}^3 P_L(k_{\text{NL}})/2\pi^2 = 1$ ($k_{\text{NL}}(z=0) \simeq 0.25 h \text{ Mpc}^{-1}$ in the fiducial cosmology); with this definition, C_s^2 is of order unity.

Next, consider $O = \delta$ correlated with a second-order operator $O' = O'^{[2]}$ in the halo field, i.e.

$$\begin{aligned} \langle [O'^{[2]}[\delta_\infty]](\mathbf{k})\delta_\Lambda(\mathbf{k}') \rangle = & \text{Diagram 1} \\ & + \text{Diagram 2} \end{aligned} \quad (3.17)$$

Here, there are two contributions, one of which involves an unregularized loop. This contribution is absorbed by a counterterm to O' that is $\propto \delta$ (the part of the diagram left of the dotted line),

$$[O'^{[2]}](\mathbf{k}) = O'^{[2]}(\mathbf{k}) - 2 \int_{|\mathbf{p}| > \Lambda_{\text{in}}} S_{O'^{[2]}}(\mathbf{p}, \mathbf{k} - \mathbf{p}) F_2(-\mathbf{p}, \mathbf{k}) P_L(p) \delta(\mathbf{k}) . \quad (3.18)$$

By absorbing the term in the correlator that scales as $P_L(p_1)$ as $p_1 \rightarrow 0$, Eq. (3.18) ensures that the renormalization conditions in Eq. (3.12) are satisfied for $O'^{[2]}$ and $l = 1$ [30]. Consider $O' = \delta^2$. In this case, Eq. (3.18) evaluates to a formally divergent constant multiplied by δ which is simply subtracted. In case of $O' = K^2$, there is a contribution with nontrivial scaling in k , which in the limit of $k \ll p$ however becomes analytic with a leading contribution $\propto k^2$, so that this contribution in Eq. (3.18) is effectively absorbed by subtracting a higher-derivative counterterm $k^2 \delta(\mathbf{k})$ (see also Appendix B). Once Eq. (3.18) is employed, one again finds agreement between the two correlators in Eq. (3.7) for $O' = O'^{[2]}$, $O = \delta$.

Notice that the first contribution in Eq. (3.17) would also involve an unregularized loop integral if one were to send $\Lambda_{\text{in}} \rightarrow \infty$, leading to a mismatch in the MAP relation, as the corresponding loop is cut at Λ in the second correlator in Eq. (3.7). Unlike the second contribution in Eq. (3.17), however, this loop integral cannot be absorbed by a counterterm to $[O']$ due to its different structure. Hence, the cutoff in the initial conditions is essential.

Next, for $O' = O'^{[3]}$ we have

$$\begin{aligned} \langle [O'^{[3]}[\delta_\infty]](\mathbf{k})\delta_\Lambda(\mathbf{k}') \rangle = & \text{Diagram 1} \\ & + \text{Diagram 2} \end{aligned} \quad (3.19)$$

Here, one similarly obtains a counterterm

$$[O'^{[3]}](\mathbf{k}) = O'^{[3]}(\mathbf{k}) - 3 \int_{|\mathbf{p}| > \Lambda_{\text{in}}} S_{O'^{[3]}}(\mathbf{p}, -\mathbf{p}, \mathbf{k}) P_L(p) \delta(\mathbf{k}) , \quad (3.20)$$

which again either is given by δ multiplied by a formally divergent constant (for $O'^{[3]} \in \{\delta^3, \delta K^2, K^3\}$) or analytic terms (for $O'^{[3]} = O_{\text{td}}$). This counterterm absorbs the contribution $\propto P_L(p_1)$ in $\langle O'^{[3]}(\mathbf{k}) \delta^{(1)}(\mathbf{p}_1) \rangle$ (Eq. (3.12) for $O'^{[3]}$ and $l = 1$), which would violate the tree-level scaling of 0.

Finally, we turn to the cross-correlation between two quadratic operators. There is a single contribution at leading order, i.e.

$$\langle [O'^{[2]}[\delta_\infty]](\mathbf{k}) O^{[2]}[\delta_\Lambda](\mathbf{k}') \rangle \Big|_{\text{LO}} = \text{Diagram} . \quad (3.21)$$

This contribution does not involve any unregularized loop integrals. At NLO, we can distinguish eight contributions. Four of these do not have to be regularized: they are

$$\langle [O'^{[2]}[\delta_\infty]](\mathbf{k}) O^{[2]}[\delta_\Lambda](\mathbf{k}') \rangle \Big|_{\text{NLO}} \supset \text{Four Diagrams} . \quad (3.22)$$

Notice that if one were to send $\Lambda_{\text{in}} \rightarrow \infty$, all diagrams here would contain unregularized loop integrals. Of these, the two diagrams on the last line would moreover lead to a mismatch in Eq. (3.7) which cannot be absorbed by counterterms, analogously to the first contribution in Eq. (3.17) discussed above.

The other four NLO diagrams need to be regularized for any value of Λ_{in} . The parts to be regularized are indicated with dotted lines, where the counterterms (which we do not

write for simplicity) absorb the part of the diagram to the left of the dotted line. They are

$$\left\langle [O'^{[2]}[\delta_\infty]](\mathbf{k}) O^{[2]}[\delta_\Lambda](\mathbf{k}') \right\rangle \Big|_{\text{NLO}} \supset$$

(3.23)

The third diagram in this equation is already absorbed by the counterterm in Eq. (3.18). The remaining three are removed by counterterms to $[O'^{[2]}]$ that are proportional to second-order operators $\tilde{O}^{[2]}$ (the first two of which have similar structure as Eq. (3.16) and Eq. (3.18), respectively). These three counterterms ensure the renormalization conditions Eq. (3.12) for $O' = O'^{[2]}$ and $l = 2$ [30].

This reasoning can be extended analogously to higher orders. The conclusion is that, once a cutoff in the initial conditions is imposed, all differences between the two types of correlators appearing on the left- and right-hand sides [Eq. (3.7)] of the maximum-a-posteriori point of Eq. (3.2) are absorbed by counterterms to the operators $[O']$ appearing in the renormalized halo bias expansion.

In Appendix B, we explicitly compute Eq. (3.2) for $O = O' = \delta$ to illustrate this reasoning quantitatively. We also show there that the remaining residuals in Eq. (3.2) can indeed be absorbed by counterterms, while this does not hold if one were to set $\Lambda_{\text{in}} \rightarrow \infty$.

4 Numerical implementation

All numerical tests presented below are based on the same set of N-body simulations used in [2], which were presented in [33]. They are generated using GADGET-2 [34] for a flat Λ CDM cosmology with parameters $\Omega_{\text{m}} = 0.3$, $n_{\text{s}} = 0.967$, $h = 0.7$, and $\sigma_8 = 0.85$, a box size of $L = 2000 h^{-1} \text{Mpc}$, and 1536^3 dark matter particles of mass $M_{\text{part}} = 1.8 \times 10^{11} h^{-1} M_{\odot}$. Two realizations are available, which we refer to as “run 1” and “run 2.” Dark matter halos were subsequently identified at different redshifts as spherical overdensities [35–37] applying the Amiga Halo Finder algorithm [38, 39] with an overdensity threshold of 200 times the background matter density. Given that the EFT approach should apply to any physical tracer, we expect the same conclusions for other halo definitions, e.g. friends-of-friends. We present results for four logarithmic mass bins, each at three redshifts.

Our lowest mass bin ranges from $10^{12.5} h^{-1} M_{\odot}$ to $10^{13} h^{-1} M_{\odot}$. The halos in this bin contain 18 or more member particles, while the mean mass corresponds to 30 particles. Halos with fewer than 30 particles can not necessarily be reliably identified with bound structures at this mass, so results on the bias and stochastic parameters for this mass bin should be taken with a grain of salt. Nevertheless, the evolution of the collection of particles making up these low-mass halos is still governed by local dynamics, so we expect the general bias expansion to also describe such poorly resolved halos, and hence lead to an unbiased estimate of σ_8 .

We employ two different approaches to generate the forward-evolved matter field to be used in the construction of the bias operators entering the likelihood. The first is to generate particle positions using second-order Lagrangian perturbation theory (2LPT) at the desired final redshift. We employ the 2LPTic code [40, 41], the same code used to generate the initial conditions of the full N-body simulations at $z_{\text{ini}} = 99$, and refer to this as “2LPT density field.” The second is to generate 2LPT particle positions at $z_{\text{ini}} = 99$, and perform an N-body simulation using the same settings as the simulations described above, evolved to the desired redshift. We refer to this as “N-body density field.” In both cases, we only populate modes with $k \leq \Lambda_{\text{in}}$ when the initial, linear displacement field is sampled in the 2LPTic code. In order to generate grid representations of density fields, we assign particles to grids of size 512^3 using a leading-order Fourier-Taylor expansion as described in Appendix C. We choose this assignment scheme rather than cloud-in-cell as its kernel shape is much closer to the desired sharp- k filter, avoiding the need for first assigning to a high-resolution grid. The same assignment scheme is used for halos.

Notice that for each value of Λ_{in} , we need to generate density fields for a range of σ_8 . For this reason, we only generated N-body density fields for a single value of $\Lambda_{\text{in}} = 0.1 h \text{ Mpc}^{-1}$. Specifically, the σ_8 values are

$$\begin{aligned} \sigma_8 &\in \{0.65, 0.75, 0.80, 0.83, 0.85, 0.87, 0.90, 0.95, 1.00, 1.10, 1.20\} \quad (2\text{LPT}) , \\ \sigma_8 &\in \{0.78, 0.83, 0.85, 0.87, 0.92\} \quad (\text{N-body}) , \end{aligned} \quad (4.1)$$

where $\sigma_8 = \sigma_8^{\text{fid}} = 0.85$ is the value used for the simulations of [33] that provide our ground truth.

At fixed Λ_{in} , halo sample, and redshift, we find the profile likelihood $-2 \ln P^{\text{prof}}(\sigma_8^i)$ by searching for the maximum in the $\{b_1, \sigma_{\epsilon}, \sigma_{\epsilon,2}\}$ space, employing the MINUIT algorithm [42] as described in [2]. This procedure results in a set of values $\{\sigma_8^i, -2 \ln P^{\text{prof}}(\sigma_8^i)\}_i$ which we find is fit well by a parabola in all cases (we disregard a small number of isolated cases where the minimization failed to converge). The best-fit value $\hat{\sigma}_8$ is given by the location of the minimum of the best-fit parabola, while the estimated 1σ error on $\hat{\sigma}_8$ is given by the inverse square-root of the curvature of the parabolic fit. For convenience, we phrase results in terms of

$$\hat{\alpha} \equiv \frac{\hat{\sigma}_8}{\sigma_8^{\text{fid}}} \quad (4.2)$$

below, so that $\hat{\alpha} = 1$ corresponds to a perfectly unbiased inference of σ_8 . We emphasize that the quoted error on $\hat{\sigma}_8$ or $\hat{\alpha}$ does not include any residual cosmic variance, and is essentially purely governed by the halo stochasticity which appears in the variance of the likelihood. It is worth noting that the error reported on $\hat{\sigma}_8$ also includes the degeneracy between the bias parameters which are marginalized over, such as b_1 , and $\hat{\sigma}_8$.

Before moving on to the results, we justify our choice of $k_{\text{max}} = \Lambda = \Lambda_{\text{in}}$. The left panel of Fig. 1 shows the ratio of power spectra of the evolved matter density field using 2LPT and

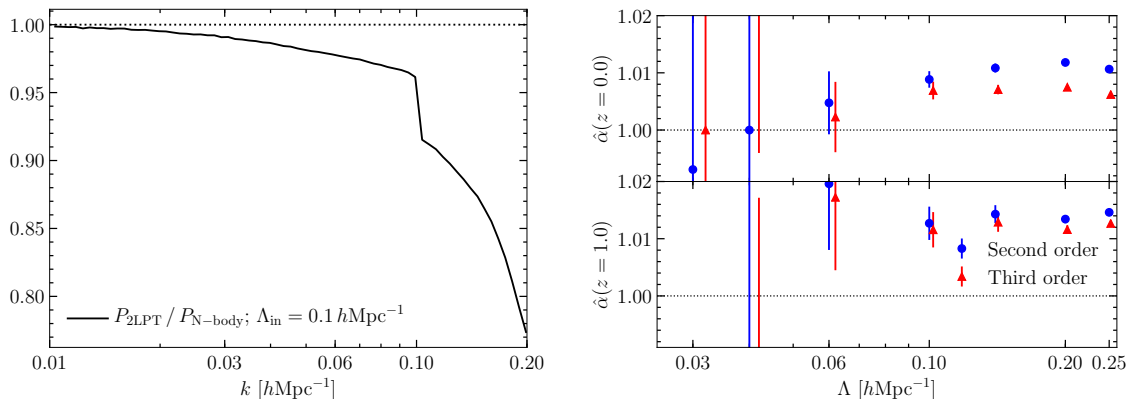


Figure 1. *Left panel:* Ratio of power spectra of the evolved matter density field at $z = 0$ for 2LPT and N-body when a momentum cutoff of $\Lambda_{\text{in}} = 0.1 \, h \, \text{Mpc}^{-1}$ is employed. *Right panel:* Maximum-likelihood (ML) values for α [Eq. (4.2)] from the profile likelihood applied to subsampled N-body particles with mean number density $\bar{n}_m = 0.01 (h \, \text{Mpc}^{-1})^3$. Results are based on the 2LPT matter density field and second- or third-order bias expansions, as labeled. The top (bottom) panel shows results at $z = 0$ ($z = 1$).

N-body forward evolution as described above. In both cases, a cutoff of $\Lambda_{\text{in}} = 0.1 \, h \, \text{Mpc}^{-1}$ is employed. We see that the disagreement between 2LPT and N-body rapidly worsens for $k > \Lambda_{\text{in}}$. This is because the modes with $k > \Lambda_{\text{in}}$ are exclusively excited by nonlinear evolution, with leading contributions that are progressively higher order as k/Λ_{in} grows; specifically, modes with $k > n\Lambda_{\text{in}}$ are only generated at $(n+1)$ -th order in perturbations. Since the 2LPT density field is only correct up to second order in perturbations, this leads to a worse description of the density field at $k > \Lambda_{\text{in}}$. For this reason, we conservatively choose to only use modes in the evolved density fields with momenta less or equal to Λ_{in} , corresponding to setting $k_{\text{max}} = \Lambda = \Lambda_{\text{in}}$.

5 Results

5.1 Test on N-body particles

Before turning to halos, we begin with a simple test case of a trivially biased tracer. Specifically, we construct a tracer density field by randomly subsampling N-body particles to a desired number density \bar{n}_m . This “tracer” is thus perfectly linearly biased with respect to the full, nonlinear N-body density field, and allows us to test the accuracy of the 2LPT matter forward model in terms of the σ_8 inference.

The right panel of Fig. 1 shows the resulting maximum-likelihood (ML) value $\hat{\alpha}$ as a function of $\Lambda_{\text{in}} = \Lambda = k_{\text{max}}$, at redshifts $z = 0$ (top) and $z = 1$ (bottom). We show results for both the second- and third-order bias expansions where, in case of a perfect matter forward model, one expects all bias parameters apart from b_1 to be consistent with zero.

Several aspects of these results are noteworthy: (i) The overall accuracy of σ_8 for subsampled N-body particles is on the order of 1% up to $\Lambda = 0.25 \, h \, \text{Mpc}^{-1}$, with a slightly better performance in case of third-order bias. This indicates that the bias parameters absorb some of the deficiencies of the 2LPT forward model. (ii) We see convergence toward $\Lambda \rightarrow 0$ at $z = 0$, as expected. (iii) The accuracy in σ_8 is not improved toward higher redshift. This

appears to indicate that the displacement contributions to the 2LPT density field that the σ_8 inference builds on are not closer to those in the N-body density field at $z = 1$ compared to $z = 0$. It would be interesting to explore whether this is due to numerical reasons or an effect that is physically expected.

One further notices from the right panel of Fig. 1 that the error bars on $\hat{\alpha}$ grow rapidly as Λ is reduced to below $0.06 h \text{ Mpc}^{-1}$. This is due to two reasons. First, at fixed simulation volume, the number of available modes rapidly shrinks toward smaller Λ . Second, the shape of the matter power spectrum changes: while $P_L(k) \propto k^{-1.5}$ at $k \simeq 0.2 h \text{ Mpc}^{-1}$, it gradually becomes shallower toward lower k , with $P_L(k) \sim \text{const}$ at $k \simeq 0.02 h \text{ Mpc}^{-1}$. As argued in [24], the EFT likelihood is based on different scalings with wavenumber of the deterministic (contained in $\delta_{h,\text{det}}$) and stochastic contributions (contained in $\sigma^2(k)$), which are in turn controlled by the power-law index of $P_L(k)$. As one reduces Λ to values approaching $0.02 h \text{ Mpc}^{-1}$, the effective index of $P_L(k)$ approaches zero (since modes with $k \ll \Lambda$ contribute fairly little due to their small number), at which point all contributions become degenerate. In order to counteract this effect, one would require either enormous simulation volumes, or simulations with non- Λ CDM forms of $P_L(k)$ that do not have a turnover, such that the power spectrum index remains significantly negative for small k . The latter would indeed provide interesting possibilities to investigate the convergence properties rigorously.

We conclude from the test on subsampled N-body particles that we do not expect σ_8 inference from halo catalogs based on the 2LPT density field to be more accurate than $\sim 1\%$.

5.2 Second-order bias

We now turn to the application to halo catalogs, beginning with the second-order bias expansion. Fig. 2 shows results at $z = 0$ for different halo mass bins, and the two simulation realizations in each case. These give a rough indication of the expected cosmic variance error. We again see the expected convergence behavior as $\Lambda \rightarrow 0$. At $\Lambda = 0.1 h \text{ Mpc}^{-1}$, σ_8 is recovered to within 7% for all mass bins. The quantitative results are summarized in Tab. 1. Notice that the impact of the higher-derivative contribution $\sigma_{\epsilon,2}$ to the noise is numerically very small. We have found that fixing $\sigma_{\epsilon,2} = 0$ in the minimization leads to negligible shifts in the maximum-likelihood values for σ_8 . This is in keeping with the theoretical expectation that the higher-derivative stochasticity is less relevant than higher-order bias terms [24].

We have already discussed the rapidly growing error bars for $\Lambda < 0.06 h \text{ Mpc}^{-1}$, which are due to the limited information available on those scales for a Λ CDM power spectrum. In case of halos, there is also a limit on the information on small scales: due to their finite number density, there is a cross-over scale k_{st} where $b_1^2 P_L(k_{\text{st}}) = 1/\bar{n}_h$, with \bar{n}_h being the mean number density of halos. Modes with $k > k_{\text{st}}$ are dominated by the stochasticity of halos, and we do not expect significant additional information from including such modes [24] (in fact, one expects additional stochastic corrections to the likelihood to become relevant on those scales, potentially leading to a bias in σ_8). The scale k_{st} is marked by the vertical lines for each halo sample in Fig. 2.

Fig. 2 also shows the result when using the matter density field from N-body rather than 2LPT, for $\Lambda = 0.1 h \text{ Mpc}^{-1}$. The results show that the ML value of σ_8 is shifted to lower values, reducing the bias in σ_8 relative to the 2LPT one in almost all cases. Again, this is as expected physically.

We next turn to the evolution with redshift, shown in Fig. 3 for the same mass bins and run 1. For most mass bins, the deviation of $\hat{\alpha}$ from 1 grows toward higher redshift. This is in contrast to the reach of perturbation theory, which is expected to extend to higher

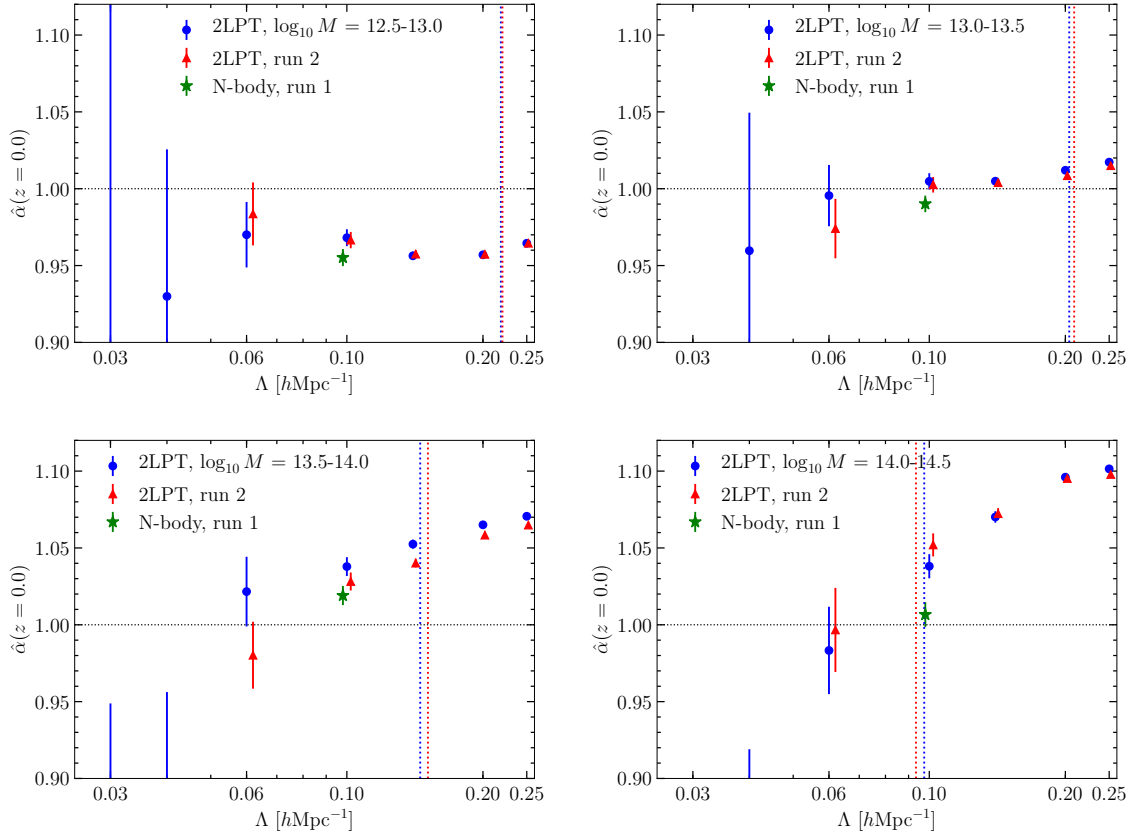


Figure 2. ML values for α using the second-order bias expansion as a function of $\Lambda = k_{\text{max}} = \Lambda_{\text{in}}$ at $z = 0$. Shown here are different mass bins each for run 1 and 2 (in the legend of these and the following plots we drop the units on M , which is always understood to be in units of $h^{-1}M_{\odot}$). Values $\Lambda < 0.06 h \text{ Mpc}^{-1}$ are only available for run 1, while the results using an N-body forward-evolved matter density field are only available for $\Lambda = 0.1 h \text{ Mpc}^{-1}$. The vertical dotted lines indicate the scale $\Lambda = k_{\text{st}}$ where $\bar{n}_h b_1^2 P_L(k_{\text{st}}) = 1$ in each case; no significant further information is expected on scales much smaller than this.

wavenumbers at higher redshifts. To understand this result, recall that the discrepancy in σ_8 is dominated by higher-order bias contributions (since we have seen that the 2LPT matter forward model shifts $\hat{\alpha}$ only at the 1% level). While the higher-order bias operators themselves are relatively suppressed by powers of $D_{\text{norm}}(z)$ at higher redshifts, where $D_{\text{norm}}(z) = D(z)/D(0)$ and $D(z)$ is the linear growth factor, the increase in their coefficients, i.e. the higher-order bias parameters, with redshift might in fact more than compensate for this suppression when considering halos within a fixed mass range. To investigate this, we can make the very rough approximation that higher-order bias parameters are proportional to $b_1^L \equiv b_1 - 1$. This approximation is motivated by the “Lagrangian local-in-matter-density” assumption, coupled with thresholding or excursion-set pictures (see Sec. 2.1–2.2 in [21]). Under these assumptions, all higher-order bias parameters are controlled by powers of b_1^L .

While very rough, and not expected to be accurate for actual halos [43–47], this approximation gives us a means of testing the source of the increasing deviation in σ_8 with redshift. Fig. 4 shows a scatter plot of $\hat{\alpha}$ against the combination expected to control the higher-order

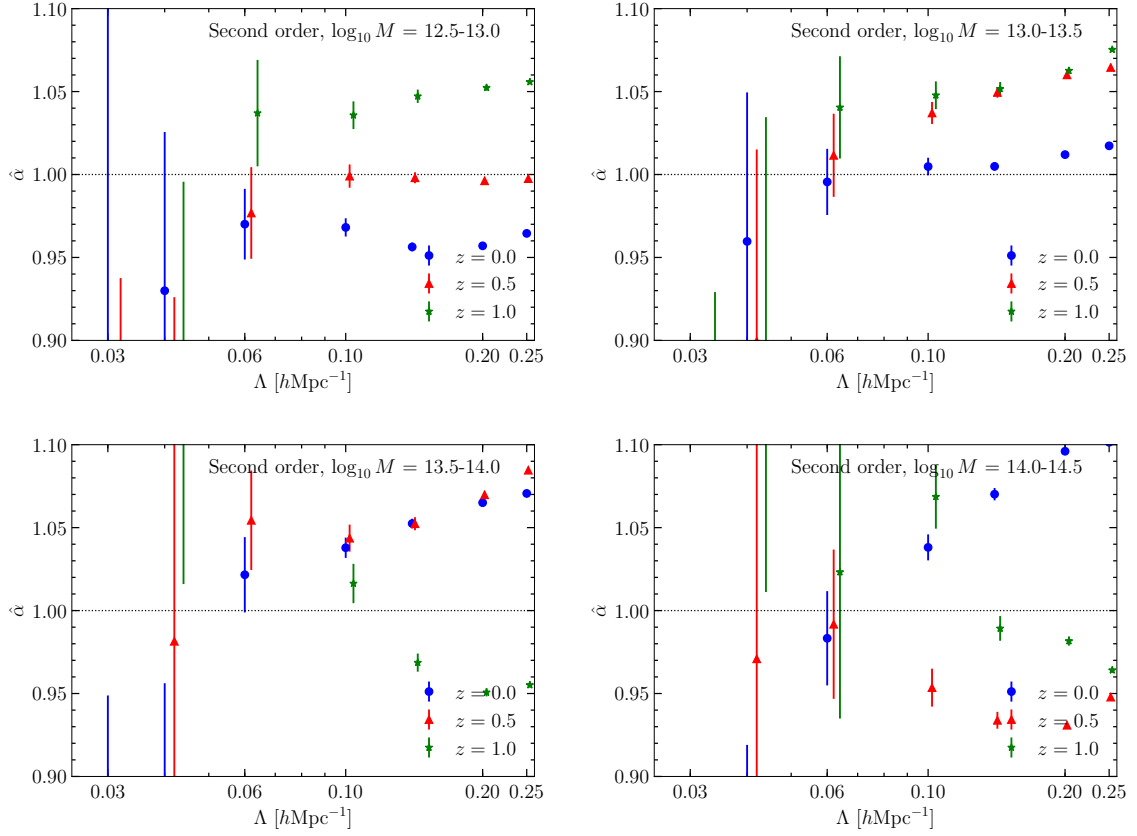


Figure 3. ML values for α using second-order bias expansion as a function of $\Lambda = k_{\max} = \Lambda_{\text{in}}$. Different panels show the four mass bins, each at different redshifts for run 1.

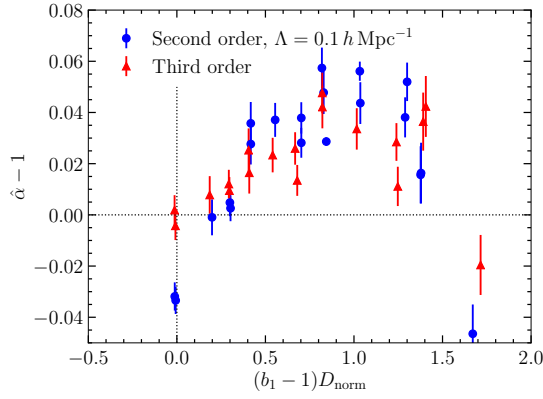


Figure 4. Fractional systematic error in σ_8 , i.e. ML values for $\alpha - 1$ for all halo mass bins and redshifts, including those shown in Fig. 3 and Fig. 7, respectively, plotted against $(b_1 - 1)D_{\text{norm}}$, where $D_{\text{norm}}(z) = D(z)/D(0)$. The latter quantity is a very rough estimate of higher-order bias corrections (see discussion in text), and shows a clear correlation with the relative bias in σ_8 , $\hat{\alpha} - 1$.

bias contributions, namely $(b_1(z) - 1)D_{\text{norm}}(z)$. Here, b_1 is taken as the maximum-likelihood

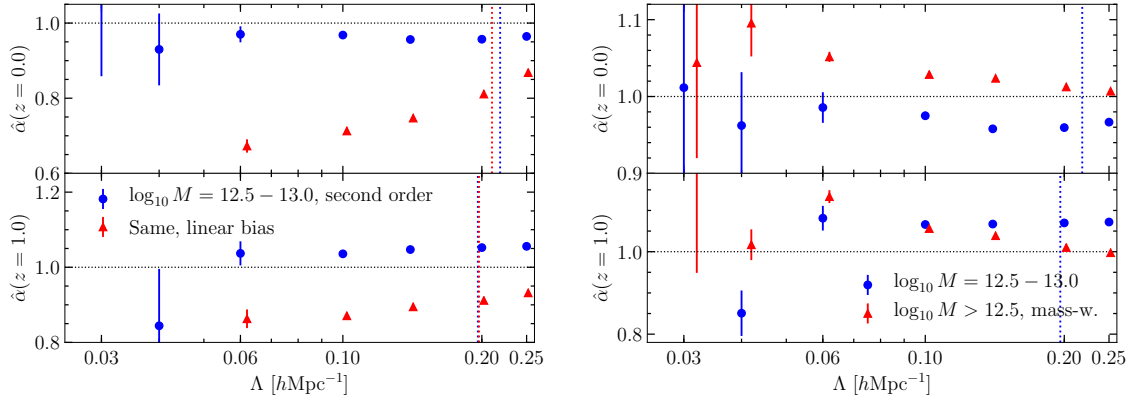


Figure 5. *Left panel:* ML values for α for linear and second-order bias expansions. The linear bias expansion leads to a significantly larger discrepancy in the inferred σ_8 value. *Right panel:* results for mass-weighted halos with $\log_{10}(M/h^{-1}M_{\odot}) > 12.5$ and using the second-order bias expansion.

value for the true σ_8 for the corresponding halo sample and redshift, while D_{norm} is computed in the simulation cosmology. We show results for second-order (blue) and third-order bias expansions (red, discussed in the next section) for all mass bins and redshifts, but at fixed $\Lambda = 0.1 h \text{ Mpc}^{-1}$. The correlation of $\hat{\alpha} - 1$ with $(b_1 - 1)D_{\text{norm}}$ is clearly visible. This lends strong support to the conjecture that the residual bias in σ_8 is due to higher-order bias contributions which scale nontrivially with mass and redshift. The results from third-order bias in the next section will provide further independent evidence for this conjecture.

Before we move on, two further tests are shown in Fig. 5: the left panel compares the result of linear bias with second-order bias for the lowest-mass bin, $\log_{10}(M/h^{-1}M_{\odot}) \in [12.5, 13.0]$. Clearly, linear bias performs much worse, which is as expected. The right panel shows the result for mass-weighting all halos with $\log_{10}(M/h^{-1}M_{\odot}) > 12.5$. The error bars shrink significantly due to the reduced stochasticity, as has been found previously [48, 49] and is expected within the halo model [50]. The bias in the central σ_8 value is comparable to the case of unweighted halos in mass bins. We conclude that, while mass weighting can significantly reduce halo stochasticity, it does not by itself substantially reduce the effect of higher-order bias corrections. Note however that these conclusions might depend on the lower mass cut used.

Redshift	Mass range $\log_{10} M [h^{-1} M_{\odot}]$	$100(\hat{\alpha} - 1)$ (run 1)	$100(\hat{\alpha} - 1)$ (run 2)	b_1	σ_{ε}^2 [Poisson]	$\sigma_{\varepsilon,2}/\sigma_{\varepsilon}$ [[$h^{-1}\text{Mpc}$] 2]
0	[12.5-13.0]	-3.2 ± 0.6	-3.3 ± 0.5	0.99	1.18	7.6
0.5	[12.5-13.0]	-0.1 ± 0.7	—	1.26	1.16	-0.3
1	[12.5-13.0]	3.6 ± 0.8	2.8 ± 0.8	1.68	1.03	1.5
0	[13.0-13.5]	0.5 ± 0.5	0.3 ± 0.5	1.30	1.05	8.8
0.5	[13.0-13.5]	3.7 ± 0.7	—	1.72	0.99	4.5
1	[13.0-13.5]	4.8 ± 0.8	5.7 ± 0.8	2.35	0.92	3.7
0	[13.5-14.0]	3.8 ± 0.6	2.8 ± 0.6	1.70	0.93	7.3
0.5	[13.5-14.0]	4.4 ± 0.8	—	2.34	0.90	3.7
1	[13.5-14.0]	1.6 ± 1.2	1.6 ± 1.1	3.25	0.90	4.1
0	[14.0-14.5]	3.8 ± 0.8	5.2 ± 0.8	2.29	0.87	4.1
0.5	[14.0-14.5]	-4.6 ± 1.1	—	3.16	0.88	4.0
1	[14.0-14.5]	6.9 ± 1.9	4.3 ± 1.8	4.37	0.93	3.8

Table 1. Summary of results for the second-order bias expansion and $k_{\text{max}} = \Lambda = \Lambda_{\text{in}} = 0.1 h \text{ Mpc}^{-1}$ for different mass bins and redshifts; for $z = 0.5$, only results for run 1 are available. The fractional deviation of the maximum-likelihood σ_8 , $\hat{\alpha} - 1$, is quoted in percent; results from run 1 and run 2 are shown individually with estimated 68% confidence-level error bars. b_1 and stochastic amplitudes are reported for the fiducial $\sigma_8 = \sigma_8^{\text{fid}}$ and averaged over both runs. The stochastic variance σ_{ε}^2 is scaled to the Poisson expectation for the given halo sample, as described in App. A of [2]. The last column shows the ratio of the higher-derivative stochastic amplitude to the leading one, indicating the scale associated with the expansion of $\sigma^2(k)$ in k .

5.3 Third-order bias

We next turn to results using the third-order bias expansion, with the list of operators given in Eq. (2.6). The results are summarized in Tab. 2 (for $\Lambda = 0.1 h \text{ Mpc}^{-1}$), and are shown as function of Λ in Fig. 6, comparing to the second-order bias case for each mass bin (at $z = 0$ and for run 1 in all cases). We find that the bias in σ_8 is reduced for all mass bins and redshifts, in some cases substantially. For many samples, the bias is under 2% and hence approaching the bias found when subsampling DM particles (Fig. 1). That is, a significant part of the residual misestimation of σ_8 might be explained by the deficiency of our matter forward model (i.e. 2LPT); we also show results at $\Lambda = 0.1 h \text{ Mpc}^{-1}$ using the N-body density field, which indeed moves $\hat{\alpha}$ even closer to unity.

Fig. 7 shows the result (third-order bias only) as a function of redshift. We generally see the same trend as in the second-order case, namely that the discrepancy in the estimated α grows toward higher redshift. This indicates that the residual discrepancy in σ_8 is indeed due to higher-order bias terms, at least in the case of highly biased tracers, and is another very important test of theoretical consistency. In Fig. 4, we also show the fractional deviation in σ_8 , $\hat{\alpha} - 1$, obtained from the third-order bias expansion at $\Lambda = 0.1 h \text{ Mpc}^{-1}$ as a function of $(b_1 - 1)D_{\text{norm}}$. A clear correlation can again be seen, with the overall deviation being smaller than in the second-order case.

Redshift	Mass range $\log_{10} M [h^{-1} M_{\odot}]$	$100(\hat{\alpha} - 1)$ (run 1)	$100(\hat{\alpha} - 1)$ (run 2)	b_1	σ_{ε}^2 [Poisson]	$\sigma_{\varepsilon,2}/\sigma_{\varepsilon}$ [[$h^{-1} \text{ Mpc}$] 2]
0	[12.5-13.0]	0.2 ± 0.6	-0.4 ± 0.6	0.99	1.17	8.2
0.5	[12.5-13.0]	0.8 ± 0.7	—	1.24	1.16	-0.2
1	[12.5-13.0]	2.5 ± 0.8	1.6 ± 0.8	1.67	1.03	1.4
0	[13.0-13.5]	1.2 ± 0.6	0.9 ± 0.5	1.29	1.05	8.8
0.5	[13.0-13.5]	2.3 ± 0.7	—	1.70	0.99	4.4
1	[13.0-13.5]	4.2 ± 0.8	4.8 ± 0.8	2.34	0.91	4.0
0	[13.5-14.0]	2.6 ± 0.6	1.3 ± 0.6	1.67	0.93	7.2
0.5	[13.5-14.0]	3.4 ± 0.8	—	2.31	0.89	3.8
1	[13.5-14.0]	4.2 ± 1.2	3.6 ± 1.1	3.29	0.90	4.5
0	[14.0-14.5]	1.1 ± 0.8	2.8 ± 0.7	2.24	0.86	4.7
0.5	[14.0-14.5]	-2.0 ± 1.2	—	3.22	0.88	4.5
1	[14.0-14.5]	-8.3 ± 2.1	-10.4 ± 2.1	4.49	0.93	3.6

Table 2. Summary of results for $\Lambda = 0.1 h \text{ Mpc}^{-1}$ and third-order bias. The columns are the same as in Tab. 1.

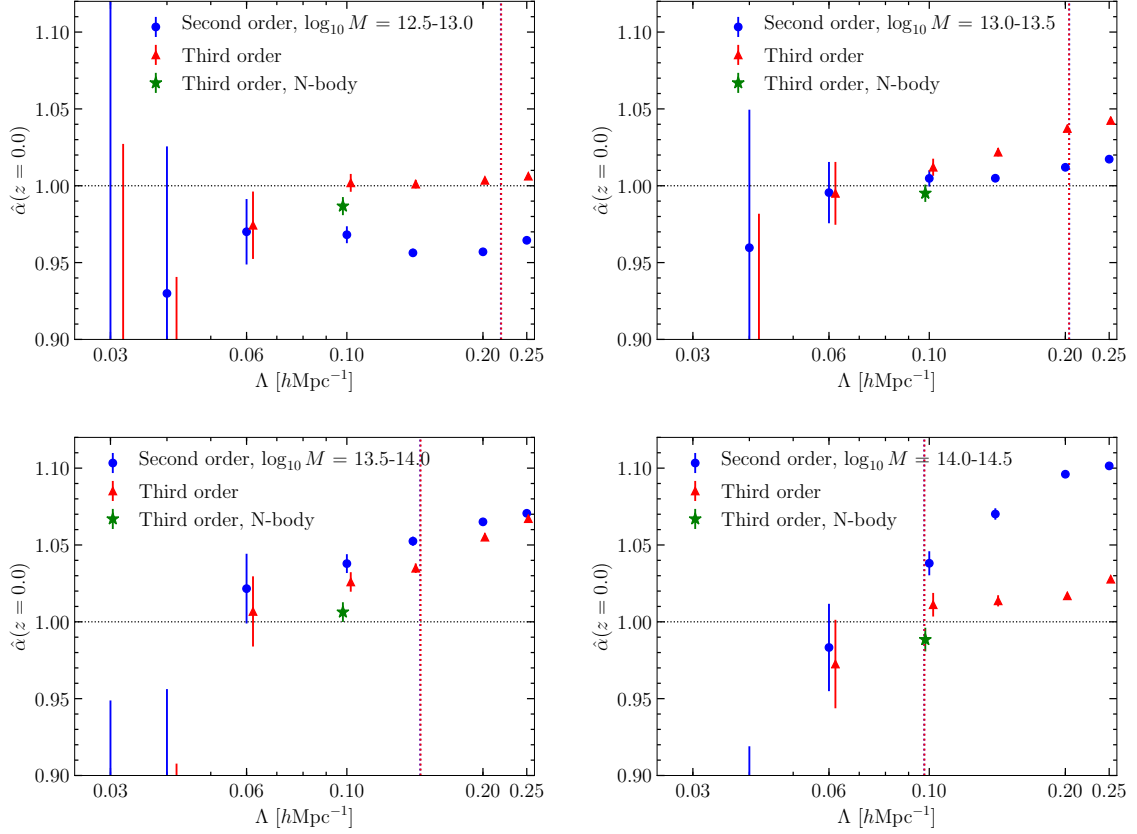


Figure 6. ML values for α as a function of $\Lambda = k_{\text{max}} = \Lambda_{\text{in}}$ for run 1 at $z = 0$. Shown here are different mass bins each for second- and third-order bias expansions (the former being the same results as shown in Fig. 2). Also shown is the third-order result when using the N-body instead of 2LPT density field (only $\Lambda = 0.1 h\text{Mpc}^{-1}$).

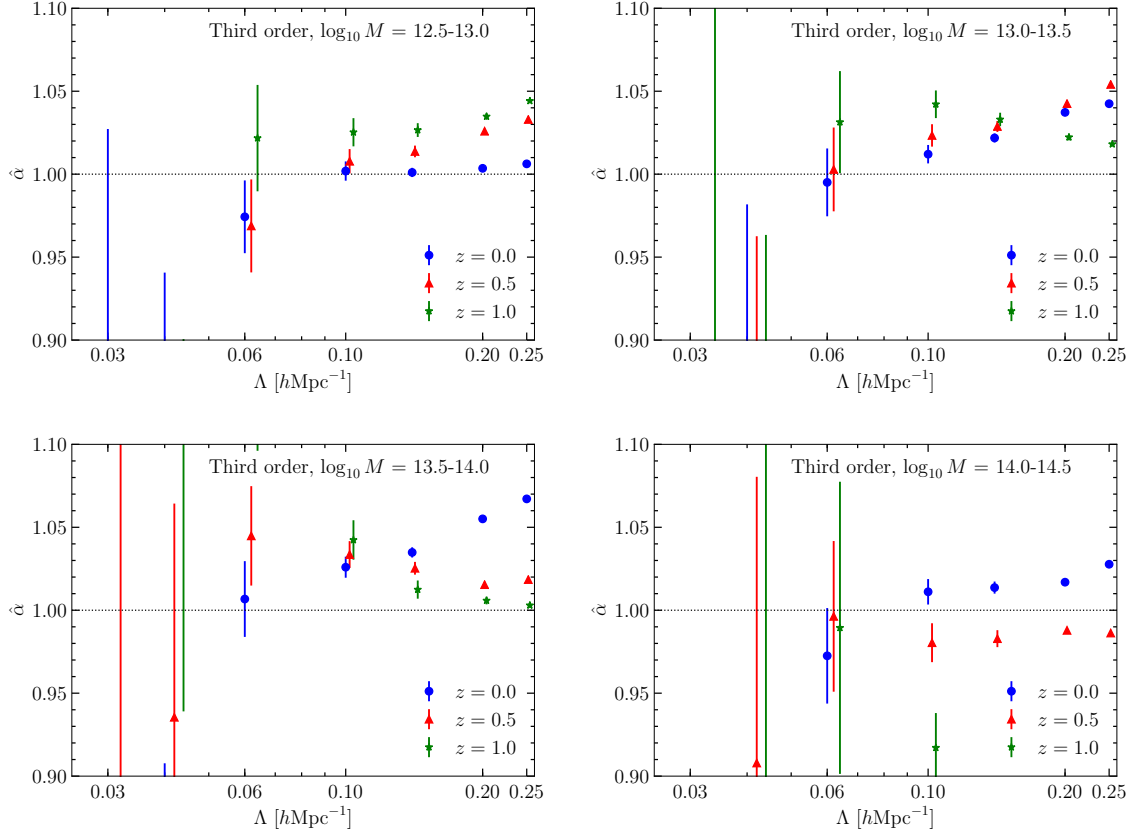


Figure 7. ML values for α using the third-order bias model as a function of $\Lambda = k_{\max} = \Lambda_{\text{in}}$. Different panels show the four mass bins, each at different redshifts for run 1.

5.4 Halo density field

After having presented the inference of σ_8 from the EFT likelihood, we now present some results on the predicted, deterministic halo density field $\delta_{h,\text{det}}$, cf. Eq. (2.1), specifically its power spectrum and cross-correlation coefficient with the actual halo density field $\delta_h(\mathbf{k})$. This is the deterministic halo field obtained using our forward model, which consists of the matter forward model plus bias fields, after inserting the maximum-likelihood bias coefficients at the fiducial value of σ_8 .

We start from the ansatz

$$\delta_h(\mathbf{k}) = \delta_{h,\text{det}}(\mathbf{k}) + \varepsilon(\mathbf{k}) . \quad (5.1)$$

We now assume that the noise field $\varepsilon(\mathbf{k})$ is a Gaussian random field with zero mean and power spectrum

$$\langle \varepsilon(\mathbf{k}) \varepsilon(\mathbf{k}') \rangle' = P_\varepsilon(k) = P_\varepsilon^{\{0\}} + P_\varepsilon^{\{2\}} k^2 . \quad (5.2)$$

When integrating out the noise field with this power spectrum, one obtains the conditional likelihood of Eq. (2.2), as shown in [1]. Further, the constants $P_\varepsilon^{\{0,2\}}$ can be obtained directly from the constants $\sigma_\varepsilon, \sigma_{\varepsilon,2}$ of the likelihood [2]:

$$P_\varepsilon^{\{0\}} = \frac{L_{\text{box}}^3}{N_g^6} \sigma_\varepsilon^2 ; \quad P_\varepsilon^{\{2\}} = 2 \frac{L_{\text{box}}^3}{N_g^6} \sigma_\varepsilon \sigma_{\varepsilon,2} . \quad (5.3)$$

At the order we work in throughout this paper, these assumptions on $\varepsilon(\mathbf{k})$ are consistent with the EFT likelihood [24].

Eq. (5.1) and the Gaussianity of ε then allow us to derive the relation between the power spectra of δ_h and $\delta_{h,\text{det}}$, denoted as $P_{hh}(k)$ and $P_{\text{det,det}}(k)$, respectively, as well as their cross-correlation coefficient, $r_{h,\text{det}}(k)$:

$$\begin{aligned} P_{hh}(k) \Big|_{\text{Gaussian noise}} &= P_{\text{det,det}}(k) + P_\varepsilon(k) \\ r_{h,\text{det}}(k) \Big|_{\text{Gaussian noise}} &= \left(1 - \frac{P_\varepsilon(k)}{P_{hh}(k)} \right)^{1/2} . \end{aligned} \quad (5.4)$$

The left panel of Fig. 8 compares both of these quantities with the measured halo power spectrum (top) and correlation coefficient with $\delta_{h,\text{det}}$ (bottom; this is inferred via $r_{h,\text{det}}^{\text{meas}} = P_{h,\text{det}} / \sqrt{P_{hh} P_{\text{det,det}}}$); in case of the power spectrum, the ratio is shown.

In each case, we choose the lowest-mass halo sample at $z = 0$, which is the least noisy sample, and our reference cutoff value $\Lambda = 0.1 h \text{ Mpc}^{-1}$. Clearly, Eq. (5.4) matches the measurements quite well. The right panel of Fig. 8 shows a histogram of the effective noise, $\delta_h(\mathbf{x}) - \delta_{h,\text{det}}(\mathbf{x})$, for the same two fields. This is computed in real space on the 512^3 grid where all fields are represented, after both fields have been sharp- k filtered at the cutoff Λ . In the limit of infinite volume, this histogram shows the 1-point probability distribution for the residual field $\delta_h(\mathbf{x}) - \delta_{h,\text{det}}(\mathbf{x})$. Both results show that the Gaussian noise assumption is an excellent approximation on the scales probed.

We next turn to the cross-correlation coefficient $r_{h,\text{det}}(k)$ for different bias expansions. This was studied in detail in [19]. One expects that adding additional bias terms should improve the correlation between $\delta_{h,\text{det}}$ and the actual halo field δ_h . We can determine $r_{h,\text{det}}(k)$ simply by using the measured $P_{hh}(k)$ and the inferred maximum-likelihood values of $\sigma_\varepsilon, \sigma_{\varepsilon,2}$. The result is shown in Fig. 9 for different bias expansions. We now choose the maximum cutoff

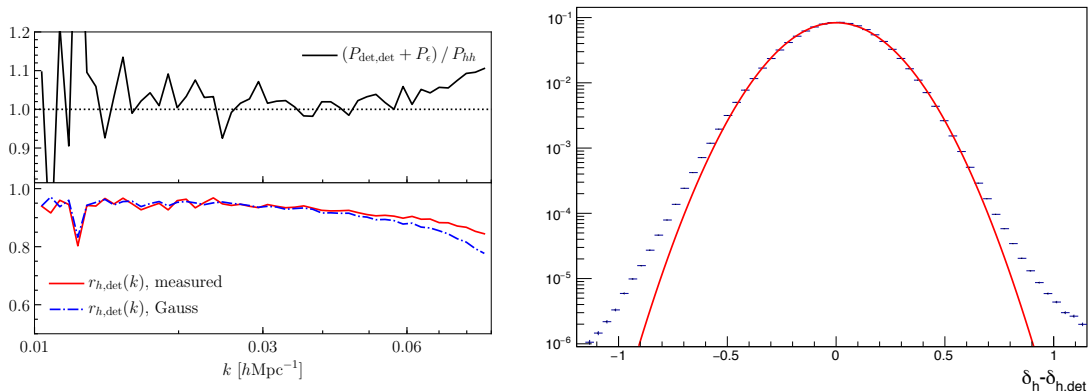


Figure 8.

Properties of the noise $\delta_h - \delta_{h,\text{det}}$. We show results for the reference cutoff value employed in the analysis, $\Lambda = 0.1 h \text{ Mpc}^{-1}$. *Left panel:* accuracy of the Gaussian-noise assumption, cf. Eq. (5.4), in the halo power spectrum (top panel) and the cross-correlation coefficient (bottom panel), both for halos with $\log_{10}(M/h^{-1}M_\odot) \in [12.5 - 13]$ at $z = 0$. Clearly, on the range of scales probed, the halo power spectrum and cross-correlation coefficient between the halo density field δ_h and the deterministic prediction $\delta_{h,\text{det}}$ are well described by Eq. (5.4). *Right panel:* normalized histogram of $\delta_h - \delta_{h,\text{det}}$ for the same halo sample and deterministic model. The solid line shows a Gaussian fit. A logarithmic scale is chosen in order to increase the visibility of the non-Gaussian tails. The Gaussian approximation is excellent.

value considered in this paper, $\Lambda = 0.25 h \text{ Mpc}^{-1}$, in order to test how much the higher-order bias contributions improve the cross-correlation on smaller scales. The linear-bias expansion here includes the leading higher-derivative term. Clearly, including second-order bias terms significantly increases the cross-correlation of $\delta_{h,\text{det}}$ with δ_h , in agreement with the findings of [19] based on a slightly different forward model. On the other hand, going to third order in the bias expansion only mildly improves the cross-correlation. In the previous section, we saw however that including third-order bias terms substantially improves the cosmological parameter estimates (in this case, σ_8 or \mathcal{A}_s). Thus, we conclude that the cross-correlation coefficient between data and model is not necessarily indicative of the quality of inferred cosmological parameters. As an example for how this can arise, consider an overall rescaling of the model prediction by a function $f(k)$. This does not change the correlation coefficient with the data or the truth, but it clearly impacts cosmological parameters inferred from the model by changing the amplitude and shape of the linear power spectrum that leads to the apparent best match with the data.

6 Conclusions

We have presented results on the inference of σ_8 from a rest-frame halo catalog using the EFT likelihood. This inference is completely based on nonlinear information that is protected by the equivalence principle and that is necessary to break the bias- σ_8 degeneracy. The EFT likelihood isolates precisely those parts of the likelihood $P(\delta_h | \{b_O, \sigma_a\}, \sigma_8, \dots)$ of a biased tracer density field δ_h that are uncertain, by making use of a full nonlinear matter forward model. That is, no perturbative expansion of the matter density field is necessary.

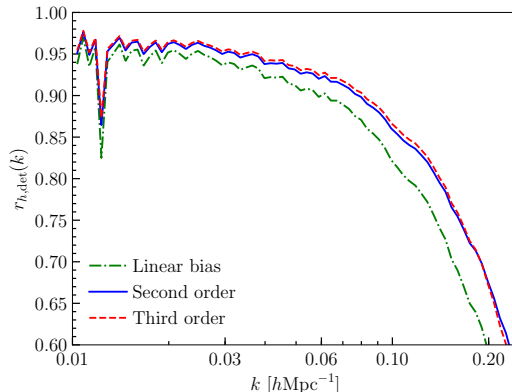


Figure 9. Cross-correlation coefficient between δ_h and $\delta_{h,\text{det}}$ as inferred using Eq. (5.4) for linear (including higher-derivative), second-order, and third-order bias expansions. Here, results are shown for the highest cutoff $\Lambda = 0.25 h \text{ Mpc}^{-1}$. The cross-correlation is improved significantly when going from linear to second-order bias, after which the improvement is small.

In contrast to previous work, we impose a cutoff on the momenta of the initial density perturbations, that is, before the perturbations are evolved forward under gravity. We show that this is crucial to regularize certain loop contributions that are otherwise not under control (Sec. 3), which we conjecture to be responsible for the biased σ_8 estimate reported in [2].

Our numerical results, presented in Sec. 5, show the expected convergence behavior as a function of scale, both for second-order and third-order bias. At the reference scale of $\Lambda = 0.1 h \text{ Mpc}^{-1}$, and excluding the most highly biased sample (i.e. $\log_{10} M > 10^{14} h^{-1} M_\odot$ at $z = 1$, with $b_1 \simeq 4.4$), σ_8 is recovered to within 6 % for the second-order bias expansion, and 4 % for the third-order bias expansion. To our knowledge, this is the *most precise inference of cosmological parameters from purely nonlinear information in biased tracers of large-scale structure* demonstrated to date—albeit fixing the phases and other cosmological parameters.

We present strong indications that the residual bias in σ_8 is due to higher-order bias terms, which is expected in the context of the EFT likelihood. Interestingly, due to the scaling of the bias parameters, these corrections do not necessarily decrease toward higher redshifts. This fact applies much more broadly to cosmology inference from biased tracers, such as via the power spectrum and bispectrum, and suggests that systematic errors from higher-order bias terms are roughly controlled by $b_1 - 1$, at least for halos.

Given that the expected convergence behavior for σ_8 is seen, there are several immediate applications of the EFT likelihood, which we leave to future work:

- Continue the bias expansion and likelihood to higher order in perturbations by including the field-dependent noise covariance [27];
- Implement the likelihood in a forward-modeling framework which samples the phases of the initial conditions;
- Apply the likelihood to measure bias parameters of halos or other tracers in simulations where phases are known, leading to the optimal cancelation of cosmic variance in bias measurements.

Finally, the connection to observations will require the incorporation of redshift-space distortions. As shown recently by Ref. [51], this is in principle straightforward within the EFT likelihood framework, by transforming the deterministic field $\delta_{h,\text{det}}$ to redshift space. We leave an implementation of this to future work as well.

Acknowledgments

We thank Alexandre Barreira, Andrija Kostić, Minh Nguyen, Marcel Schmittfull and Marko Simonović for helpful discussions, and Franz Elsner and Minh Nguyen for collaboration on previous work leading up to these results. We further thank Titouan Lazeyras for supplying us with the N-body and 2LPT codes used to generate initial conditions for the simulations our results are based on. FS thanks Oliver Hahn, Cornelius Rampf and the OCA, Nice, for hospitality while this work was being completed.

GC and FS acknowledge support from the Starting Grant (ERC-2015-STG 678652) “GrInflaGal” of the European Research Council. GL acknowledges financial support from the ILP LABEX (under reference ANR-10-LABX-63) which is financed by French state funds managed by the ANR within the Investissements d’Avenir programme under reference ANR-11-IDEX-0004-02. This work was supported by the ANR BIG4 project, grant ANR-16-CE23-0002 of the French Agence Nationale de la Recherche. This work is done within the Aquila Consortium.⁵

⁵<https://aquila-consortium.org>

A Deriving the maximum-a-posteriori relation

In this appendix we review how to obtain the maximum-a-posteriori relation of Eqs. (3.1)–(3.2). The logarithm of the likelihood is given in Eq. (2.2). The “data” $\delta_h(\mathbf{k})$ are obtained for a given set of initial conditions $\hat{\delta}_{\text{in}} = \hat{\delta}_{\text{in},\infty}$ (i.e., as discussed in Sec. 3, the initial conditions are not cut at Λ_{in}). In the perturbative description, δ_h is then a linear combination of renormalized operators $[O]$ constructed from $\hat{\delta}_{\text{in},\infty}$, and a set of bias parameters b_O^h . The “model” is instead given by Eqs. (2.1), (3.5), i.e.

$$\delta_{h,\text{det}} = \sum_O b_O O[\delta_\Lambda] , \quad (\text{A.1})$$

where

$$\delta_\Lambda(\mathbf{k}) = W_\Lambda(\mathbf{k}) \delta_{\text{fwd}} \left[\hat{\delta}_{\text{in},\Lambda_{\text{in}}} \right] (\mathbf{k}) \quad \text{and} \quad \hat{\delta}_{\text{in},\Lambda_{\text{in}}} = W_{\Lambda_{\text{in}}}(\mathbf{k}) \hat{\delta}_{\text{in}} . \quad (\text{A.2})$$

That is, while in the application to real data one must perform an inference of the initial conditions as well, we here instead fix δ_{in} in Eqs. (A.1)–(A.2) to be equal to the set of initial conditions $\hat{\delta}_{\text{in}}$ we have used to generate the data. Our likelihood then becomes only a function of cosmological and bias parameters. Since the bias parameters b_O appear only quadratically, it is straightforward to take the derivative of the logarithm of the likelihood with respect to them and look for the maximum. The relation one obtains is

$$\sum_{\mathbf{k} \neq 0}^{k_{\text{max}}} \frac{1}{\sigma^2(k)} \delta_h(\mathbf{k}) O(-\mathbf{k}) = \sum_{\mathbf{k} \neq 0}^{k_{\text{max}}} \frac{1}{\sigma^2(k)} \sum_{O'} b_{O'} O'(\mathbf{k}) O(-\mathbf{k}) \quad \forall O . \quad (\text{A.3})$$

Importantly, $\sum_{\mathbf{k} \neq 0}^{k_{\text{max}}} 1/\sigma^2(k)$ defines a scalar product given that $\sigma^2(k)$ is strictly nonnegative. Together with the fact that Eq. (A.3) must hold for any shape of the linear power spectrum, this allows us to write the maximum-a-posteriori relation at a fixed \mathbf{k} , i.e.

$$\delta_h(\mathbf{k}) O(-\mathbf{k}) = \sum_{O'} b_{O'} O'(\mathbf{k}) O(-\mathbf{k}) \quad \forall O . \quad (\text{A.4})$$

We can then multiply this equality on both sides by the Gaussian prior on the initial conditions and functionally integrate over $\hat{\delta}_{\text{in}}$. Using translational invariance, we arrive at Eq. (3.1).

B Maximum-a-posteriori relation for $O = O' = \delta$

In this appendix, we explicitly compute the left- and right-hand sides of Eq. (3.2) for $O = \delta$:

$$\langle \delta_\Lambda(\mathbf{k}) \delta_h(\mathbf{k}') \rangle = \sum_{O'} b_{O'} \langle \delta_\Lambda(\mathbf{k}) O'[\delta_\Lambda](\mathbf{k}') \rangle . \quad (\text{B.1})$$

As in App. A, we will denote the halo bias parameters on the left-hand side with b_O^h , while the bias parameters in the likelihood on the right-hand side will be denoted as b_O . In the following, we explicitly include both the cutoff Λ on the final density field as well as that imposed on the initial density field, Λ_{in} . Throughout, we assume $k < \min(\Lambda_{\text{in}}, \Lambda)$ so that we can set factors of $W_\Lambda(\mathbf{k})$, $W_{\Lambda_{\text{in}}}(\mathbf{k})$ to unity.

Left-hand side: Using the results from Sec. 4.1 of [21], and paying attention to the cutoff in the initial conditions following Sec. 3, we can write

$$\begin{aligned}
\langle \delta_\Lambda(\mathbf{k}) \delta_h(\mathbf{k}') \rangle' &= b_1^h \left[P_L(k) + P_{mm}^{\text{NLO}}(k; \Lambda_{\text{in}}, \infty) \right] \\
&+ 2 \sum_{O'[2]} b_{O'}^h \int_{\mathbf{p}} S_{O'}(\mathbf{p}, \mathbf{k} - \mathbf{p}) F_2(\mathbf{p}, \mathbf{k} - \mathbf{p}) P_L(p) P_L(|\mathbf{k} - \mathbf{p}|) W_{\Lambda_{\text{in}}}(\mathbf{p}) W_{\Lambda_{\text{in}}}(\mathbf{k} - \mathbf{p}) \\
&+ 4 \sum_{O'[2]} b_{O'}^h \int_{\mathbf{p}} S_{O'}(\mathbf{p}, \mathbf{k} - \mathbf{p}) F_2(\mathbf{k}, -\mathbf{p}) P_L(p) P_L(k) \\
&+ \frac{2}{5} b_{\text{td}}^h f_{\text{NLO}}(k) P_L(k) - b_{\nabla^2 \delta}^h k^2 P_L(k) \\
&+ \text{counterterms} ,
\end{aligned} \tag{B.2}$$

where $\sum_{O'[2]}$ denotes a sum over all bias operators that start at second order, and

$$\begin{aligned}
P_{mm}^{\text{NLO}}(k; \Lambda_{\text{in}}, \Lambda'_{\text{in}}) &\stackrel{\Lambda_{\text{in}} \leq \Lambda'_{\text{in}}}{=} 2 \int_{\mathbf{p}} [F_2(\mathbf{p}, \mathbf{k} - \mathbf{p})]^2 P_L(p) P_L(|\mathbf{k} - \mathbf{p}|) W_{\Lambda_{\text{in}}}(\mathbf{p}) W_{\Lambda_{\text{in}}}(\mathbf{k} - \mathbf{p}) \\
&+ 3 P_L(k) \int_{\mathbf{p}} F_3(\mathbf{p}, -\mathbf{p}, \mathbf{k}) P_L(p) \left[W_{\Lambda_{\text{in}}}(\mathbf{p}) + W_{\Lambda'_{\text{in}}}(\mathbf{p}) \right]
\end{aligned} \tag{B.3}$$

is the NLO (1-loop) contribution to the cross-correlation between forward-evolved matter density fields with two different initial cutoffs $\Lambda_{\text{in}}, \Lambda'_{\text{in}}$ (and we have assumed $\Lambda_{\text{in}} \leq \Lambda'_{\text{in}}$ without loss of generality). Thus, $P_{mm}^{\text{NLO}}(k; \Lambda_{\text{in}}, \infty)$ is the NLO cross-correlation between forward-evolved matter density fields *with* and *without* cutoff in the initial conditions, corresponding to the contributions shown in Eq. (3.15). Further, $f_{\text{NLO}}(k)$ is defined as

$$f_{\text{NLO}}(k) = 4 \int_{\mathbf{p}} \left[\frac{[\mathbf{p} \cdot (\mathbf{k} - \mathbf{p})]^2}{p^2 |\mathbf{k} - \mathbf{p}|^2} - 1 \right] F_2(\mathbf{k}, -\mathbf{p}) P_L(p) . \tag{B.4}$$

The terms in the second (third) line of Eq. (B.2) can be identified with the first (second) term in Eq. (3.17). The first term in the fourth line corresponds to Eq. (3.19).

Right-hand side: extending App. C of [1] by the cutoff in the initial conditions, we straightforwardly obtain

$$\begin{aligned}
\sum_{O'} b_{O'} \langle \delta_\Lambda(\mathbf{k}) O'[\delta_\Lambda](\mathbf{k}') \rangle &= \left(b_1 - b_{\nabla^2 \delta} k^2 \right) \left[P_L(k) + P_{mm}^{\text{NLO}}(k; \Lambda_{\text{in}}, \Lambda_{\text{in}}) \right] \\
&+ 2 \sum_{O'[2]} b_{O'} \int_{\mathbf{p}} S_{O'}(\mathbf{p}, \mathbf{k} - \mathbf{p}) W_\Lambda(\mathbf{p}) W_\Lambda(\mathbf{k} - \mathbf{p}) \\
&\times \left[F_2(\mathbf{p}, \mathbf{k} - \mathbf{p}) P_L(p) P_L(|\mathbf{k} - \mathbf{p}|) \right. \\
&\quad \left. + \{ F_2(\mathbf{p}, -\mathbf{k}) P_L(p) + F_2(\mathbf{k} - \mathbf{p}, -\mathbf{k}) P_L(|\mathbf{k} - \mathbf{p}|) \} P_L(k) \right] .
\end{aligned} \tag{B.5}$$

The two terms in braces on the last line yield the same result, as can be see by shifting integration variables $\mathbf{p} \rightarrow \mathbf{p}' = \mathbf{k} - \mathbf{p}$. Notice that all loop integrals here are regularized, i.e. no modes with momenta greater than 2Λ or $2\Lambda_{\text{in}}$ appear.

Residual: taking the difference of left- and right-hand sides, and setting $b_O^h = b_O$ (we will see that this applies to all bias parameters except for $b_{\nabla^2 \delta}$, which absorbs additional

contributions), we have

$$\begin{aligned}
\text{Eq. (B.2)–Eq. (B.5)} &= b_1 \left[P_{mm}^{\text{NLO}}(k; \Lambda_{\text{in}}, \infty) - P_{mm}^{\text{NLO}}(k; \Lambda_{\text{in}}, \Lambda_{\text{in}}) \right] \\
&+ 2 \sum_{O' [2]} b_{O'} \int_{\mathbf{p}} S_{O'}(\mathbf{p}, \mathbf{k} - \mathbf{p}) F_2(\mathbf{p}, \mathbf{k} - \mathbf{p}) P_L(p) P_L(|\mathbf{k} - \mathbf{p}|) \\
&\quad \times [W_{\Lambda_{\text{in}}}(\mathbf{p}) W_{\Lambda_{\text{in}}}(\mathbf{k} - \mathbf{p}) - W_{\Lambda}(\mathbf{p}) W_{\Lambda}(\mathbf{k} - \mathbf{p})] \\
&+ 4 P_L(k) \sum_{O' [2]} b_{O'} \int_{\mathbf{p}} S_{O'}(\mathbf{p}, \mathbf{k} - \mathbf{p}) F_2(\mathbf{k}, -\mathbf{p}) P_L(p) \\
&\quad \times [1 - W_{\Lambda}(\mathbf{p}) W_{\Lambda}(\mathbf{k} - \mathbf{p})] \\
&+ \frac{2}{5} b_{\text{td}} f_{\text{NLO}}(k) P_L(k) \\
&+ \text{counterterms} .
\end{aligned} \tag{B.6}$$

Let us go through the residuals line by line.

(1) The residual in the first line of Eq. (B.6) scales as

$$\begin{aligned}
(1) : \quad &P_L(k) \int_{\mathbf{p}} F_3(\mathbf{p}, -\mathbf{p}, \mathbf{k}) P_L(p) [1 - W_{\Lambda_{\text{in}}}(\mathbf{p})] \\
&= \int_{|\mathbf{p}| > \Lambda_{\text{in}}} F_3(\mathbf{p}, -\mathbf{p}, \mathbf{k}) P_L(p) \sim \frac{k^2}{k_{\text{NL}}^2} P_L(k) .
\end{aligned} \tag{B.7}$$

That is, only modes $|\mathbf{p}| > \Lambda_{\text{in}}$ contribute. In the last, approximate scaling we have assumed that $k \ll k_{\text{NL}}$, which is the wavenumber around which the integrand peaks, and used the fact that $F_3(\mathbf{p}, -\mathbf{p}, \mathbf{k}) \propto k^2/p^2$ in the regime where $k \ll p \sim k_{\text{NL}}$. In Sec. 3, we showed that this residual is absorbed by the counterterm in Eq. (3.16). The finite contribution $\propto C_s^2$ can be absorbed by the higher-derivative bias $b_{\nabla^2 \delta}$, which at this order is perfectly degenerate with the C_s^2 contribution. Notice that this particular residual is absent when *not* cutting on the initial modes, but is precisely absorbed by a counterterm when the cutoff Λ_{in} is employed.

(2) The next contribution (second and third lines of Eq. (B.6)) is

$$\begin{aligned}
(2) : \quad &2 \sum_{O' [2]} b_{O'} \int_{\mathbf{p}} S_{O'}(\mathbf{p}, \mathbf{k} - \mathbf{p}) F_2(\mathbf{p}, \mathbf{k} - \mathbf{p}) P_L(p) P_L(|\mathbf{k} - \mathbf{p}|) \\
&\quad \times [W_{\Lambda_{\text{in}}}(\mathbf{p}) W_{\Lambda_{\text{in}}}(\mathbf{k} - \mathbf{p}) - W_{\Lambda}(\mathbf{p}) W_{\Lambda}(\mathbf{k} - \mathbf{p})] .
\end{aligned} \tag{B.8}$$

Clearly, this residual vanishes if $\Lambda_{\text{in}} = \Lambda$. On the other hand, if we set $\Lambda_{\text{in}} \rightarrow \infty$, corresponding to no cutoff in the initial conditions, then modes with $|\mathbf{p}| > \Lambda$ or $|\mathbf{k} - \mathbf{p}| > \Lambda$ contribute to the residual. Following similar reasoning as above, one roughly expects the result to scale as

$$(2), \Lambda_{\text{in}} \rightarrow \infty : \quad \int_{|\mathbf{p}| > \Lambda} \frac{k^2}{p^2} [P_L(p)]^2 \sim 2\pi^2 \frac{k^2}{k_{\text{NL}}^5} , \tag{B.9}$$

although this scaling is not actually attained in practice (Fig. 10).

(3) We next consider the third contribution (fourth and fifth lines of Eq. (B.6)),

$$\begin{aligned}
(3) : \quad &4 P_L(k) \sum_{O' [2]} b_{O'} \int_{\mathbf{p}} S_{O'}(\mathbf{p}, \mathbf{k} - \mathbf{p}) F_2(\mathbf{k}, -\mathbf{p}) P_L(p) \\
&\quad \times [1 - W_{\Lambda}(\mathbf{p}) W_{\Lambda}(\mathbf{k} - \mathbf{p})] .
\end{aligned} \tag{B.10}$$

This contribution corresponds to the counterterm in Eq. (3.18). For $O' = \delta^2$, it yields a contribution of $P_L(k)$ multiplied by a formally divergent constant, while for $O' = K^2$ there is an additional term scaling as $k^2 P_L(k)$ for $k \ll p$, to which the reasoning made for residual (1) applies.

(4) Finally, we have the sixth line of Eq. (B.6),

$$(4) : \quad \frac{2}{5} b_{\text{td}} f_{\text{NLO}}(k) P_L(k) . \quad (\text{B.11})$$

This residual remains due to the second-order bias expansion adopted in this derivation. As argued in [1], this contribution fairly accurately follows a scaling of $k^2 P_L(k)$, allowing it to be approximately absorbed by the higher-derivative bias term $\propto b_{\nabla^2 \delta}$ as well. Notice that residual (4) is taken into account by the operator O_{td} when going to a third-order bias expansion, which could partially explain the significantly improved results obtained for the third-order bias.

To summarize, choosing a cutoff Λ_{in} in the initial conditions introduces an additional residual, (1), at the MAP level, while it removes the residual (2). Both in terms of scaling with k as well as absolute size, one might expect residual (1) ($\propto k^2 P_L(k)$) to be more important than residual (3) ($\propto k^2$). However, the scaling of residual (1) is precisely of the form expected for the counterterm, to within a few percent, and can hence be absorbed in $b_{\nabla^2 \delta}$ to the same precision. On the other hand, residual (2) scales nontrivially with k , and cannot be absorbed by a counterterm, as is illustrated in the left panel of Fig. 10. This is due to the different support of the integrand of residual (2) as compared to the other residuals, as well as cancelations between modes with $p > \Lambda$ and $p < \Lambda$ which no longer happen when a cut on $|\mathbf{k} - \mathbf{p}|$ is present. These results illustrate the conclusions of Sec. 3: all UV-sensitive loop integrals that remain after a cutoff Λ_{in} in the initial conditions is imposed can be absorbed by counterterms in the bias expansion, while this does not hold in the absence of the cutoff Λ_{in} .

C Fourier-Taylor density assignment

In order to obtain halo and matter density representations from a set of discrete halo or particle positions $\{\mathbf{x}_p\}$, a density assignment has to be used. Since we are interested in obtaining fields that are sharp- k filtered, the density assignment kernel should be as close as possible to a sharp- k filter, defined as being precisely unity for modes below the cutoff, and zero otherwise. One possibility to achieve this is to first perform an assignment on a high-resolution grid using a standard kernel such as cloud-in-cell (CIC), and to then apply a sharp- k filter on the density grid in Fourier space. This is the approach followed for the results in [2]. An alternative, more memory-efficient method is the Fourier-Taylor assignment scheme presented in [52] (see also [53]) which we employ for the results presented in this paper.

The exact representation of the Fourier-space density field of a set of point-like particles is given by

$$\delta(\mathbf{k}) \stackrel{\mathbf{k} \neq 0}{=} m \sum_p e^{-i\mathbf{x}_p \cdot \mathbf{k}} = m \sum_p e^{-i[\mathbf{x}_{g,p} + \mathbf{s}_p] \cdot \mathbf{k}} , \quad (\text{C.1})$$

where $m = N_g^3/N_p$ is the grid mass, given by the number of grid cells N_g^3 divided by the number of particles N_p , and we only consider nonzero wavenumbers as $\delta(\mathbf{k} = 0) = 0$. In the second equality, we have introduced a finite grid and separated each particle position \mathbf{x}_p into

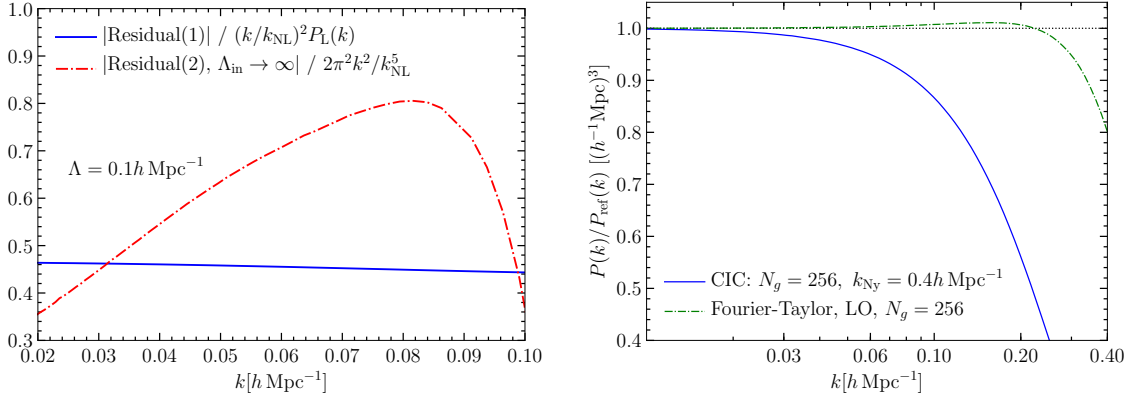


Figure 10. *Left panel:* Residuals in the MAP relation for $O = \delta$, Eq. (B.1). Shown are ratios of residuals (1), for $\Lambda_{\text{in}} = \Lambda$, and (3), for $\Lambda_{\text{in}} = \infty$, to their expected scalings. While residual (3) is smaller numerically, it shows a nontrivial scaling which cannot be absorbed by other counterterms. On the other hand, residual (1) scales as $k^2 P_L(k)$ to within a few percent, and can thus be absorbed by $b_{\nabla^2 \delta}$. *Right panel:* Effective assignment kernels squared for CIC (solid) and leading-order Fourier-Taylor (dot-dashed), determined by measuring the ratio of power spectra to those from a high-resolution grid. See Appendix C for details.

the position of the center of the grid cell $\mathbf{x}_{g,p}$ containing the particle, and the displacement \mathbf{s}_p of the particle from the cell center. Since $|\mathbf{s}_p| < r_{\text{cell}}/2$, the quantity $\mathbf{s}_p \cdot \mathbf{k}$ is at most of order k/k_{Ny} , where k_{Ny} is the Nyquist frequency of the grid. Since, in our application, all Fourier modes above some cutoff $\Lambda < k_{\text{Ny}}$ are set to zero (usually we choose Λ to be at most $1/3$ to $1/2$ of k_{Ny}), $\mathbf{s}_p \cdot \mathbf{k}$ is a small quantity for all Fourier modes that are kept.

Hence, we can expand Eq. (C.1) in $\mathbf{s}_p \cdot \mathbf{k}$ to obtain

$$\begin{aligned} \delta(\mathbf{k}) &\stackrel{k \neq 0}{=} m \sum_p e^{-i\mathbf{x}_{g,p} \cdot \mathbf{k}} \left[1 - i\mathbf{s}_p \cdot \mathbf{k} + \frac{1}{2}(\mathbf{s}_p \cdot \mathbf{k})^2 + \dots \right] \\ &= m \left[\sum_p e^{-i\mathbf{x}_{g,p} \cdot \mathbf{k}} - ik_j \cdot \sum_p e^{-i\mathbf{x}_{g,p} \cdot \mathbf{k}} s_p^j + \frac{1}{2} k_j k_l \sum_p e^{-i\mathbf{x}_{g,p} \cdot \mathbf{k}} s_p^j s_p^l + \dots \right]. \end{aligned} \quad (\text{C.2})$$

The first term here is just the Fourier transform of the density field obtained by performing a grid assignment with the nearest-grid-point (NGP) kernel. Similarly, the coefficient of $-ik_j$ in the second term, $\sum_p e^{-i\mathbf{x}_{g,p} \cdot \mathbf{k}} s_p^j$, is the Fourier transform of a Cartesian vector grid obtained by assigning the components of the displacements within the cell weighted by the NGP kernel. The third term correspondingly involves the Fourier transform of a Cartesian tensor grid. Eq. (C.2) can be implemented efficiently numerically by performing the NGP assignments in real space, and then summing the terms after transforming all grids to Fourier space. In our implementation, we keep the zeroth- as well as linear-order terms in $\mathbf{k} \cdot \mathbf{s}_p$, and refer to this as “leading-order Fourier-Taylor” assignment (while keeping only the zeroth order term in Eq. (C.2) corresponds to standard NGP assignment).

In order to test the grid assignment, we construct the matter density field from the N-body particle output at $z = 0$ and measure its power spectrum. We then take the ratio of the power spectrum measured in a low-resolution grid (256^3) to a reference result taken from a high-resolution (1024^3) CIC-assigned grid. For a perfect sharp- k filtered density field, the result should be unity for modes below the cutoff. The result is shown in the right panel

of Fig. 10, for both CIC and LO Fourier-Taylor kernels, where the Nyquist frequency of the low-resolution grid is $k_{\text{Ny}} = 0.4 h \text{ Mpc}^{-1}$. Clearly, the Fourier-Taylor assignment is much closer to the desired sharp- k filter, with deviations within a few percent up to $0.8k_{\text{Ny}}$. This correspondingly reduces the grid resolution necessary to implement a desired cutoff Λ , i.e. $k_{\text{Ny}} \gtrsim 1.2\Lambda$ is sufficient.

It is worth noting that, for the Fourier-Taylor assignment, the resulting density field is not guaranteed to satisfy $1 + \delta(\mathbf{x}) > 0$ everywhere. For the application in the EFT likelihood, this is not an issue, since there is no requirement on the positivity of $1 + \delta$. Similarly, the Fourier-Taylor assignment can be very useful whenever correlation functions of Fourier-space density fields are to be measured [53], and when the data are not regularly sampled [54].

References

- [1] F. Schmidt, F. Elsner, J. Jasche, N. M. Nguyen and G. Lavaux, *A rigorous EFT-based forward model for large-scale structure*, *Journal of Cosmology and Astro-Particle Physics* **2019** (Jan., 2019) 042, [[1808.02002](#)].
- [2] F. Elsner, F. Schmidt, J. Jasche, G. Lavaux and N.-M. Nguyen, *Cosmology Inference from Biased Tracers using the EFT-based Likelihood*, *JCAP* **2001** (2020) 029, [[1906.07143](#)].
- [3] E. Bertschinger and A. Dekel, *Recovering the full velocity and density fields from large-scale redshift-distance samples*, *ApJL* **336** (Jan., 1989) L5–L8.
- [4] O. Lahav, K. B. Fisher, Y. Hoffman, C. A. Scharf and S. Zaroubi, *Wiener Reconstruction of All-Sky Galaxy Surveys in Spherical Harmonics*, *ApJL* **423** (Mar., 1994) L93, [[astro-ph/9311059](#)].
- [5] K. B. Fisher, O. Lahav, Y. Hoffman, D. Lynden-Bell and S. Zaroubi, *Wiener reconstruction of density, velocity and potential fields from all-sky galaxy redshift surveys*, *MNRAS* **272** (Feb., 1995) 885–908, [[astro-ph/9406009](#)].
- [6] I. M. Schmoldt, V. Saar, P. Saha, E. Branchini, G. P. Efstathiou, C. S. Frenk et al., *On Density and Velocity Fields and beta from the IRAS PSCZ Survey*, *AJ* **118** (Sept., 1999) 1146–1160, [[astro-ph/9906035](#)].
- [7] P. Erdoğdu, O. Lahav, S. Zaroubi, G. Efstathiou, S. Moody, J. A. Peacock et al., *The 2dF Galaxy Redshift Survey: Wiener reconstruction of the cosmic web*, *MNRAS* **352** (Aug., 2004) 939–960, [[astro-ph/0312546](#)].
- [8] J. Jasche, F. S. Kitaura, B. D. Wandelt and T. A. Enßlin, *Bayesian power-spectrum inference for large-scale structure data*, *MNRAS* **406** (July, 2010) 60–85, [[0911.2493](#)].
- [9] J. Jasche and F. S. Kitaura, *Fast Hamiltonian sampling for large-scale structure inference*, *MNRAS* **407** (Sept., 2010) 29–42, [[0911.2496](#)].
- [10] J. Jasche, F. S. Kitaura, C. Li and T. A. Enßlin, *Bayesian non-linear large-scale structure inference of the Sloan Digital Sky Survey Data Release 7*, *MNRAS* **409** (Nov., 2010) 355–370, [[0911.2498](#)].
- [11] F.-S. Kitaura, J. Jasche and R. B. Metcalf, *Recovering the non-linear density field from the galaxy distribution with a Poisson-lognormal filter*, *MNRAS* **403** (Apr., 2010) 589–604, [[0911.1407](#)].
- [12] F.-S. Kitaura, S. Gallerani and A. Ferrara, *Multiscale inference of matter fields and baryon acoustic oscillations from the Ly α forest*, *MNRAS* **420** (Feb., 2012) 61–74, [[1011.6233](#)].
- [13] J. Jasche and B. D. Wandelt, *Bayesian physical reconstruction of initial conditions from large-scale structure surveys*, *MNRAS* **432** (June, 2013) 894–913, [[1203.3639](#)].

- [14] H. Wang, H. J. Mo, X. Yang, Y. P. Jing and W. P. Lin, *ELUCID - Exploring the Local Universe with reConstructed Initial Density field I: Hamiltonian Markov Chain Monte Carlo Method with Particle Mesh Dynamics*, *Astrophys. J.* **794** (2014) 94, [[1407.3451](#)].
- [15] M. Ata, F.-S. Kitaura and V. Müller, *Bayesian inference of cosmic density fields from non-linear, scale-dependent, and stochastic biased tracers*, *MNRAS* **446** (Feb., 2015) 4250–4259, [[1408.2566](#)].
- [16] H. Wang, H. J. Mo, X. Yang, Y. Zhang, J. Shi, Y. P. Jing et al., *ELUCID - Exploring the Local Universe with reConstructed Initial Density field III: Constrained Simulation in the SDSS Volume*, *Astrophys. J.* **831** (2016) 164, [[1608.01763](#)].
- [17] M. Ata, F.-S. Kitaura, C.-H. Chuang, S. Rodríguez-Torres, R. E. Angulo, S. Ferraro et al., *The clustering of galaxies in the completed SDSS-III Baryon Oscillation Spectroscopic Survey: cosmic flows and cosmic web from luminous red galaxies*, *MNRAS* **467** (June, 2017) 3993–4014, [[1605.09745](#)].
- [18] U. Seljak, G. Aslanyan, Y. Feng and C. Modi, *Towards optimal extraction of cosmological information from nonlinear data*, *JCAP* **12** (Dec., 2017) 009, [[1706.06645](#)].
- [19] M. Schmittfull, M. Simonović, V. Assassi and M. Zaldarriaga, *Modeling Biased Tracers at the Field Level*, *Phys. Rev.* **D100** (2019) 043514, [[1811.10640](#)].
- [20] C. Modi, M. White, A. Slosar and E. Castorina, *Reconstructing large-scale structure with neutral hydrogen surveys*, *JCAP* **1911** (2019) 023, [[1907.02330](#)].
- [21] V. Desjacques, D. Jeong and F. Schmidt, *Large-scale galaxy bias*, *PhR* **733** (Feb., 2018) 1–193, [[1611.09787](#)].
- [22] D. Baumann, A. Nicolis, L. Senatore and M. Zaldarriaga, *Cosmological non-linearities as an effective fluid*, *JCAP* **7** (July, 2012) 051, [[1004.2488](#)].
- [23] J. J. M. Carrasco, M. P. Hertzberg and L. Senatore, *The effective field theory of cosmological large scale structures*, *Journal of High Energy Physics* **9** (Sept., 2012) 82, [[1206.2926](#)].
- [24] G. Cabass and F. Schmidt, *The EFT Likelihood for Large-Scale Structure*, *JCAP* **04** (2020) 042, [[1909.04022](#)].
- [25] L. Senatore, *Bias in the effective field theory of large scale structures*, *JCAP* **11** (Nov., 2015) 007, [[1406.7843](#)].
- [26] M. Mirbabayi, F. Schmidt and M. Zaldarriaga, *Biased tracers and time evolution*, *JCAP* **7** (July, 2015) 030, [[1412.5169](#)].
- [27] G. Cabass and F. Schmidt, *The Likelihood for LSS: Stochasticity of Bias Coefficients at All Orders*, *JCAP* **07** (2020) 051, [[2004.00617](#)].
- [28] S. M. Carroll, S. Leichenauer and J. Pollack, *Consistent effective theory of long-wavelength cosmological perturbations*, *Phys. Rev.* **D90** (2014) 023518, [[1310.2920](#)].
- [29] S. S. Wilks, *The Large-Sample Distribution of the Likelihood Ratio for Testing Composite Hypotheses*, *Ann. Math. Statist.* **9** (Mar., 1938) 60–62.
- [30] V. Assassi, D. Baumann, D. Green and M. Zaldarriaga, *Renormalized halo bias*, *JCAP* **8** (Aug., 2014) 056, [[1402.5916](#)].
- [31] A. Akbar Abolhasani, M. Mirbabayi and E. Pajer, *Systematic renormalization of the effective theory of Large Scale Structure*, *JCAP* **5** (May, 2016) 063, [[1509.07886](#)].
- [32] F. Bernardeau, S. Colombi, E. Gaztanaga and R. Scoccimarro, *Large scale structure of the universe and cosmological perturbation theory*, *Phys.Rept.* **367** (2002) 1–248, [[astro-ph/0112551](#)].

- [33] M. Biagetti, T. Lazeyras, T. Baldauf, V. Desjacques and F. Schmidt, *Verifying the consistency relation for the scale-dependent bias from local primordial non-Gaussianity*, *MNRAS* **468** (July, 2017) 3277–3288, [[1611.04901](#)].
- [34] V. Springel, *The cosmological simulation code GADGET-2*, *MNRAS* **364** (Dec., 2005) 1105–1134, [[astro-ph/0505010](#)].
- [35] W. H. Press and P. Schechter, *Formation of Galaxies and Clusters of Galaxies by Self-Similar Gravitational Condensation*, *ApJ* **187** (Feb., 1974) 425–438.
- [36] M. S. Warren, P. J. Quinn, J. K. Salmon and W. H. Zurek, *Dark halos formed via dissipationless collapse. I - Shapes and alignment of angular momentum*, *ApJ* **399** (Nov., 1992) 405–425.
- [37] C. Lacey and S. Cole, *Merger Rates in Hierarchical Models of Galaxy Formation - Part Two - Comparison with N-Body Simulations*, *MNRAS* **271** (Dec., 1994) 676, [[astro-ph/9402069](#)].
- [38] S. P. D. Gill, A. Knebe and B. K. Gibson, *The evolution of substructure - I. A new identification method*, *MNRAS* **351** (June, 2004) 399–409, [[astro-ph/0404258](#)].
- [39] S. R. Knollmann and A. Knebe, *AHF: Amiga’s Halo Finder*, *ApJS* **182** (June, 2009) 608–624, [[0904.3662](#)].
- [40] M. Crocce, S. Pueblas and R. Scoccimarro, *Transients from initial conditions in cosmological simulations*, *MNRAS* **373** (Nov., 2006) 369–381, [[astro-ph/0606505](#)].
- [41] R. Scoccimarro, L. Hui, M. Manera and K. C. Chan, *Large-scale bias and efficient generation of initial conditions for nonlocal primordial non-Gaussianity*, *PhRvD* **85** (Apr., 2012) 083002, [[1108.5512](#)].
- [42] F. James and M. Roos, *Minuit: A System for Function Minimization and Analysis of the Parameter Errors and Correlations*, *Comput. Phys. Commun.* **10** (1975) 343–367.
- [43] T. Baldauf, U. Seljak, V. Desjacques and P. McDonald, *Evidence for Quadratic Tidal Tensor Bias from the Halo Bispectrum*, *Phys. Rev.* **D86** (2012) 083540, [[1201.4827](#)].
- [44] R. K. Sheth, K. C. Chan and R. Scoccimarro, *Nonlocal Lagrangian bias*, *Phys. Rev.* **D87** (2013) 083002, [[1207.7117](#)].
- [45] C. Modi, E. Castorina and U. Seljak, *Halo bias in Lagrangian Space: Estimators and theoretical predictions*, *Mon. Not. Roy. Astron. Soc.* **472** (2017) 3959–3970, [[1612.01621](#)].
- [46] T. Lazeyras and F. Schmidt, *Beyond LIMD bias: a measurement of the complete set of third-order halo bias parameters*, *JCAP* **1809** (2018) 008, [[1712.07531](#)].
- [47] M. M. Abidi and T. Baldauf, *Cubic Halo Bias in Eulerian and Lagrangian Space*, *JCAP* **1807** (2018) 029, [[1802.07622](#)].
- [48] U. Seljak, N. Hamaus and V. Desjacques, *How to Suppress the Shot Noise in Galaxy Surveys*, *Physical Review Letters* **103** (Aug., 2009) 091303, [[0904.2963](#)].
- [49] N. Hamaus, U. Seljak, V. Desjacques, R. E. Smith and T. Baldauf, *Minimizing the stochasticity of halos in large-scale structure surveys*, *PhRvD* **82** (Aug., 2010) 043515–+, [[1004.5377](#)].
- [50] F. Schmidt, *Towards a self-consistent halo model for the nonlinear large-scale structure*, *PhRvD* **93** (Mar., 2016) 063512, [[1511.02231](#)].
- [51] G. Cabass, *The EFT Likelihood for Large-Scale Structure in Redshift Space*, [2007.14988](#).
- [52] C. Anderson and M. D. Dahleh, *Rapid Computation of the Discrete Fourier Transform*, *SIAM J. Sci. Comput.* **17**(4) (1995) 913–919.
- [53] S. Colombi, A. Jaffe, D. Novikov and C. Pichon, *Accurate estimators of power spectra in N-body simulations*, *MNRAS* **393** (Feb., 2009) 511–526, [[0811.0313](#)].

- [54] G. Lavaux, *Bayesian 3D velocity field reconstruction with VIRBIuS*, *Mon. Not. Roy. Astron. Soc.* **457** (2016) 172–197, [[1512.04534](#)].